A multiscale and multiaxial model for anisotropic damage and failure of human annulus fibrosus

Abderrahman Tamoud, Fahmi Zaïri, Amar Mesbah, Fahed Zaïri

Version of Record: https://www.sciencedirect.com/science/article/pii/S0020740321002939
Manuscript_b544c8b528444ff7b1ed7c6e8a8bbce2

A multiscale and multiaxial model for anisotropic damage and failure of human annulus fibrosus

Abderrahman Tamoud[a,b], Fahmi Zaïri[a*], Amar Mesbah[b], Fahed Zaïri[c]

[a]Lille University, Civil Engineering and geo-Environmental Laboratory (ULR 4515 LGCgE), 59000 Lille, France
[b]University of Sciences and Technology Houari Boumediene, Laboratory of Advanced Mechanics, 16111 Algiers, Algeria
[c]Ramsay Générale de Santé, Hôpital privé Le Bois, 59000 Lille, France

*Corresponding author.
E-mail address: fahmi.zairi@polytech-lille.fr

Abstract

This article presents a multiscale model to predict deformation-induced damage and failure of human annulus fibrosus under multiaxial loading. In the modeling approach, formulated within the framework of nonlinear continuum mechanics, the hierarchical structure of the soft tissue is considered from the nano-sized collagen fibrils to the micro-sized oriented collagen fibers. At the macroscale, the multi-layered lamellar/inter-lamellar organization of the soft tissue is introduced by considering the effective interactions between adjacent layers. The stochastic process of progressive damage events operating at different scales of the solid phase is introduced for the extracellular matrix and the network of nano-sized fibrils/micro-sized fibers. The damage is made anisotropic due to lamellar oriented collagen fibers and special orientation distribution of the inter-fibrillar and inter-lamellar network of fibrils. The chemical-induced volumetric strain is also considered in our modeling approach to take into account the osmolarity effects along with the anisotropic time-dependent transversal deformations. The capacity of the model is discussed using a few available stretching datasets till failure along circumferential and radial directions. Model predictions under tilted stretching, biaxial stretching and shearing are also presented to illustrate further the efficiencies of our modeling approach. This work shows for the first time the directional effects on annulus mechanics and failure in relation to external loading mode, structure features, damage events and hydration.

Keywords: Multiscale; Osmolarity; Multiaxial; Damage; Failure.

Nomenclature

$\mathbf{F}$: Deformation gradient tensor
$\mathbf{L}$: Velocity gradient tensor
$\mathbf{C}$: Right Cauchy-green strain tensor
$\mathbf{E}$: Green-Lagrange strain tensor
$\boldsymbol{\sigma}$: Cauchy stress tensor
$\mathbf{P}$: First Piola-Kirchhoff stress tensor
$\mathbf{R}$: Rotational basis-change tensor
$\mathbf{I}$: Identity tensor
$\boldsymbol{x}$, $\boldsymbol{y}$, $\boldsymbol{z}$: Cartesian coordinate vectors
$\boldsymbol{a}$: Unit vector of collagen fiber
$\boldsymbol{b}$: Unit vector of collagen fibril
$\boldsymbol{n}$: Unit vector at the inter-layer interfaces
θ: Fiber angle with respect to the $\boldsymbol{xy}$-plane
ψ : Fibril angle with respect to the $\boldsymbol{az}$-plane
γ: Load angle with respect to $\boldsymbol{xz}$-plane
q: Fibril quantity
η: Fibril bundle number
$_z$: Layer thickness
m: Number of layers
ϕ: Volume fraction

W : Free energy function
p : Hydrostatic pressure
$\overline{I}$: Isochoric invariant
J : Volumetric change
λ : Stretch
λ^*: Transition stretch
κ : Shear strain

Operators

$H(\bullet)$ Heaviside
$\otimes$ Direct (outer) product
$(\bullet)^T$ Transpose
$\cdot$ Simple contraction

Abbreviations

LM: Lamellar
ILM: Inter-lamellar
ECM: Extracellular matrix
OCF: Oriented collagen fibers
NEF: Nano-sized elastic fibers

1. Introduction

The ineluctable deterioration of the intervertebral disc annulus fibrosus is a multiscale phenomenon due to the hierarchical structure of this soft tissue [1-13]. The irreversible degradation in annulus fibrosus operates from the nanoscale [14] to the macroscale [15] and results in the development of multiple cracks and tears [16-17]. There is a considerable qualitative understanding of the microstructure and chemical factors that govern the response of the soft tissue. However, the coupling between these factors and mechanics is yet far to be fully understood in annulus fibrosus.

The introduction of the tissue structure at different scales in a continuum-based modeling framework would allow to propose predictive tools for mechanical damage and failure in a physically consistent way. Over the years, macroscopic continuum-based damage models were proposed using two main approaches. The first one considers reduction factors incorporated in the free energy function [18-26]. The second one introduces an energy limiter in the expression of the free energy function [27-28]. No model until now is able to predict the multiaxial behavior of annulus fibrosus till failure and such a development remains a challenging task. The main difficulty comes from the anisotropic mechanics of a tissue with a

complex hierarchical solid phase starting from the nanoscale [12-13]. The degree of knowledge of the collagen network has considerably increased thanks to the technological advances in the imaging field [1-11]. For a physically consistent constitutive representation, an accurate structure of the solid phase must be taken into account [29] in interaction with the surrounding environment. In this regard, the fluid phase transfer by osmotic effect through the tissue solid phase affects largely the biochemical volumetric behavior [30-33]. The coupling between deformation-induced stress and swelling due to internal fluid content variation by osmosis is mandatory to quantitatively analyze the annulus fibrosus multiaxial mechanics [34] along with the failure [15].

The deterioration of the annulus fibrosus is indeed a multi-physics phenomenon since it implies biochemical degradation processes interacting in a complex manner with the external loading mode and the induced mechanical damage. A loss of electrolytic properties of extracellular matrix (ECM) proteoglycan macromolecules occurs with the tissue degeneration, which results in a decrease of osmotic pressure [35-36]. In the meantime, high mechanical loads cause tissue degenerative changes resulting in the degradation of the proteoglycan macromolecules associated with the enzymes of the ECM metalloproteinase activity [37]. The induced metabolic phenomena in the ECM cause a degradation of the osmotic properties of the annulus fibrosus associated with a decrease in water content and structure changes [38]. These changes may alter the resistance of the annulus fibrosus to the mechanical-induced crack propagation [15, 39]. Establishing annulus damage-structure-osmotic relationships is a fundamental task for a detailed understanding of the degeneration mechanisms, to reduce their effects and to potentially prevent dangerous degenerative cases from happening. For an accurate annulus behavior, the structure-chemo-mechanics relationship can only be seen by considering, in addition to the annulus stretching in the circumferential direction, representative of the disc compression mechanics, the multiaxiality of the external mechanical loading representative of the body movements [34]. The latter is the key point to better understand the origin of multi-directional micro-cracks and tears commonly observed in the annulus fibrosus [40].

In this paper, a multiscale model for deformation-induced damage and failure of annulus fibrosus is proposed by considering the structure at different scales, the micromechanical deformation processes leading to the final failure, the anisotropic nonlinear mechanics and the coupling with the osmotic effects. The proposed model, fully three-dimensional, is used to examine the multiaxial mechanics of the tissue and the directional effects. Uniaxial stretching, biaxial stretching and shearing are all being considered. The multiaxial model results are

correlated to the microstructure features, to their progressive deformation-induced changes, to the tissue volumetric behavior and to the final failure.

The paper is organized as follows. In Section 2, the annulus multiscale model is presented within the framework of nonlinear continuum mechanics. In Section 3, the model is verified for different loading paths and is used to discuss important aspects of the annulus mechanics in relation to volumetric effects and to damage accumulation in the tissue due to progressive local failure events. Section 4 closes the paper with some concluding remarks.

2. Model formulation

The following notation is used throughout the text. Tensors and vectors are respectively denoted by normal boldfaced letters and italicized boldfaced letters, while scalars and individual components of vectors and tensors are denoted by normal italicized letters. The superposed dot designates the time derivative.

2.1. Hierarchical organization of annulus fibrosus

Let us start by the presentation of the hierarchical organization of all discrete solid components. Fig. 1 presents a schematic representation of the soft tissue hierarchical structure based on earlier experimental observations starting from the intervertebral disc at the upper scale and ending to the organization of the collagen network at the microscale and at the nanoscale. The multiple-network medium is constantly immerged in a physiological solution of water and ions. At the scale of the annulus fibrosus, inter-lamellar (ILM) matrix connects fibers-reinforced lamellae (LM) such that a (concentric) multi-layered material element is formed with distinct radial and circumferential microstructure features (retaining inner gel-like disc portion, i.e. nucleus pulposus). The tangled ECM consists in very large randomly oriented proteoglycan macromolecules with glycosaminoglycan chains that have ionic imbalances and interact with the ionic components of the surrounding physiological fluid to maintain electroneutrality by osmotic effect. The micro-sized type-I oriented collagen fibers (OCF) represent up to 80% of the total volume of collagen network $\phi_{collagen}$ [1, 5, 41]. This family of fibers is described geometrically by a unit vector $\boldsymbol{a}$ in the initial configuration with respect to the global benchmark of the disc as illustrated in Fig. 2a. It is expressed in the Cartesian coordinates by:

$$\boldsymbol{a} = \cos\theta\,\boldsymbol{x} + |\sin\theta|\,\boldsymbol{y} \tag{1}$$

where θ is the fibers angle with respect to the circumferential direction.

At the nano-scale, a complex network of collagen fibrils, termed elastic fibers in the literature [1, 7, 11], exists both in the LM zone and in the ILM zone as illustrated in Fig. 1. In the LM zone, they act as inter-fibrillar connections of type-I collagen fibers (Fig. 1c). In the ILM zone, they act as inter-lamellar connections of two adjacent lamellae (Fig. 1d) [1, 4-7]. For symmetry reasons, the distribution of the nano-sized elastic fibers (NEF) is described geometrically by an angle ψ ranged from 0° to 180° with respect to the radial direction in the parallel plane of the fibers as illustrated in Fig. 2b. The unit vector $\boldsymbol{b}$ of each fibril in the initial configuration is expressed with respect to the global benchmark of the disc in the Cartesian coordinates as follows:

$$\boldsymbol{b} = \left|\cos\theta\cos\psi\right|\boldsymbol{x} + \left|\sin\theta\cos\psi\right|\boldsymbol{y} + \sin\psi\,\boldsymbol{z} \tag{2}$$

The fruitful experimental quantifications of NEF performed by Tavakoli et al. [11] are used as direct inputs of our modeling approach. Fig. 3 provides the number of NEF in the LM and ILM layers as a function of the orientation ψ. We use a Gaussian probability density function to describe these experimental trends:

$$q_\eta^{LM} = \chi_\eta^{LM} \exp\left(-\varsigma^{LM}\left(\psi-\eta\right)^2\right) \text{ and } q_\eta^{ILM} = \chi_\eta^{ILM} \exp\left(-\varsigma^{ILM}\left(\psi-\eta\right)^2\right) \tag{3}$$

where χ_η^{LM} and χ_η^{ILM} denote the respective peak values with $\eta = \{0°, 45°, 90°, 135°, 180°\}$ and, $\varsigma^{LM} = 0.05$ and $\varsigma^{ILM} = 0.11$ are two factors.

The volume fraction of a fibril in each layer *i* is given by:

$$\phi_\eta^{LM\_i} = \begin{cases} \dfrac{q_\eta^{LM} + q_\eta^{ILM}}{q^{LM}} & \eta = 0°,180° \\ \dfrac{q_\eta^{LM}}{q^{LM}} & \eta = 45°,90°,135° \end{cases} \text{ and } \phi_\eta^{ILM\_i} = \begin{cases} 0 & \eta = 0°,180° \\ \dfrac{q_\eta^{ILM}}{q^{ILM}} & \eta = 45°,90°,135° \end{cases} \tag{4}$$

where q^{LM} and q^{ILM} are the respective total number of NEF in each layer *i*:

$$q^{LM} = \sum_\eta \sum_\psi q_\eta^{LM} + \sum_{\eta=0°,180°} \sum_\psi q_\eta^{ILM} \text{ and } q^{ILM} = \sum_{\eta=45°,90°,135°} \sum_\psi q_\eta^{ILM} \tag{5}$$

Due to the presence of inter-fibrillar connections of type-I collagen fibers in LM zone, a second term appears in the first equation.

In what follows, the features of the annulus mechanics are described along with a set of constitutive equations for the solid phase behavior using a physically realistic approach accounting for microstructure organization at different scales, damage and hydration.

2.2. Free energy of the fluid phase and swelling-related changes

Local ionic diffusion is responsible for dilatation effects and nonlinear time-dependent transversal stretch response of the multi-lamellar annulus [42-45]. The derivation of the constitutive model must take into account this chemical coupling in the description of the finite-strain kinematics [46]. In this framework, the basic quantity is the deformation gradient tensor mapping material tangent vectors in their reference configuration to their actual position in the deformed configuration. It is designated here as $\mathbf{F}^i$ for each layer i of the multi-layered material element. The introduction of an intermediate (virtual) configuration assumed stress-free allows to multiplicatively decompose the deformation gradient tensor $\mathbf{F}^i$ into a chemical-induced volumetric part $\mathbf{F}^i_{chem}$ and a mechanical part $\mathbf{F}^i_{mech}$ as follows:

$$\mathbf{F}^i = \mathbf{F}^i_{chem}.\mathbf{F}^i_{mech} \tag{6}$$

in which $\mathbf{F}^i_{chem}$ is the swelling expansion due to internal fluid content variation and $\mathbf{F}^i_{mech}$ is the mechanical (isochoric) stress-producing contribution. The sequence of configurations implies also an additive split of the gradient tensor $\mathbf{L}^i$ of the spatial velocity into a chemical-induced volumetric part $\mathbf{L}^i_{chem}$ and a mechanical part $\mathbf{L}^i_{mech}$ as:

$$\mathbf{L}^i = \underbrace{\dot{\mathbf{F}}^i_{chem}.\mathbf{F}^{i^{-1}}_{chem}}_{\mathbf{L}^i_{chem}} + \underbrace{\mathbf{F}^i_{chem}.\dot{\mathbf{F}}^i_{mech}.\mathbf{F}^{i^{-1}}_{mech}.\mathbf{F}^{i^{-1}}_{chem}}_{\mathbf{L}^i_{mech}} \tag{7}$$

The determinant (Jacobian) $J^i = \det\left(\mathbf{F}^i\right) > 0$ of the deformation gradient tensor $\mathbf{F}^i$ gives:

$$J^i = J^i_{chem} J^i_{mech},\ J^i_{mech} = \det\left(\mathbf{F}^i_{mech}\right) = 1 \text{ and } J^i_{chem} = \det\left(\mathbf{F}^i_{chem}\right) \tag{8}$$

where the term J^i_{chem} represents the tissue chemical-induced volumetric change. In view of the mechanical incompressibility of all solid components (ECM, OCF and NEF), the term J^i_{mech} is equal to one. We may define the total Green-Lagrange strain tensor $\mathbf{E}^i$, the mechanical (isochoric) Green-Lagrange strain tensor $\mathbf{E}^i_{mech}$ and the chemical-induced volumetric strain ε^i_{chem}:

$$\mathbf{E}^i = \frac{1}{2}\left(\mathbf{C}^i - \mathbf{I}\right),\ \mathbf{E}^i_{mech} = \frac{1}{2}\left(\mathbf{C}^i_{mech} - \mathbf{I}\right) \text{ and } \varepsilon^i_{chem} = J^i_{chem} - 1 \tag{9}$$

where $\mathbf{I}$ is the unit tensor, $\mathbf{C}^i = \mathbf{F}^{i^T}.\mathbf{F}^i$ is the total right Cauchy-Green strain tensor and $\mathbf{C}^i_{mech} = \mathbf{F}^{i^T}_{mech}.\mathbf{F}^i_{mech}$ is the mechanical (isochoric) right Cauchy-Green strain tensor.

For each layer, the respective volume fractions of the three solid components (ECM, OCF and NEF) may be expressed as:

$$\phi^i_{ECM} = \frac{\phi^i_{ECM\_0}}{J^i_{chem}},\ \phi^i_{OCF} = \frac{\phi^i_{OCF\_0}}{J^i_{chem}} \text{ and } \phi^i_{NEF} = \frac{\phi^i_{NEF\_0}}{J^i_{chem}} \tag{10}$$

where $\phi^i_{ECM\_0}$, $\phi^i_{OCF\_0}$ and $\phi^i_{NEF\_0}$ are the initial volume fractions in each layer i.

The volume fraction of the fluid phase ϕ^i_{fluid} in each layer i is then given by:

$$\phi^i_{fluid} = 1 - \frac{\phi^i_{ECM\_0} + \phi^i_{OCF\_0} + \phi^i_{NEF\_0}}{J^i_{chem}} \tag{11}$$

The Cauchy stress tensor $\boldsymbol{\sigma}^i$, defined in the deformed configuration, is additively split into a mechanical part $\boldsymbol{\sigma}^i_{mech}$ and a chemical-induced volumetric part $\boldsymbol{\sigma}^i_{chem}$. The latter tensor is given by:

$$\boldsymbol{\sigma}^i_{chem} = \frac{\partial W^i_{chem}}{\partial J^i_{chem}} \mathbf{I} \tag{12}$$

where W^i_{chem} is the chemical-induced volumetric free energy function, due to the internal fluid content variation, expressed in the following form [47]:

$$W^i_{chem} = \phi^i_{fluid} \frac{1}{2} \frac{K_1}{K_2} \left(\exp\left(K_2 \left(J^i_{chem} - 1 \right)^2 \right) - 1 \right) \tag{13}$$

where K_1 and K_2 are material constants, K_1 and K_1/K_2 being respectively the initial and maximal volumetric stiffness values.

2.3. Free energies of the solid phase

Each individual component of the solid phase (ECM, OCF and NEF) is assumed as isotropic, homogeneous, incompressible and hyperelastic body. The mechanical Cauchy stress tensor $\boldsymbol{\sigma}^i_{mech}$ is obtained from the differentiation of the mechanical free energy function W^i_{mech} with respect to the corresponding deformation:

$$\boldsymbol{\sigma}^i_{mech} = 2\mathbf{F}^i_{mech} \cdot \frac{\partial W^i_{mech}}{\partial \mathbf{C}^i_{mech}} \cdot \mathbf{F}^{iT}_{mech} - p^i \mathbf{I} \tag{14}$$

where p^i is determined from boundary conditions.

The mechanical free energy W^i_{mech} is given as a function of the free energies of the three solid components (ECM, OCF and NEF) using the volume fraction concept:

$$W^{LM\_i}_{mech} = \phi^i_{ECM} W^i_{ECM} + \phi^i_{OCF} W^{LM\_i}_{OCF} + \phi^i_{NEF} W^{LM\_i}_{NEF} \tag{15}$$

in LM layer and,

$$W^{ILM\_i}_{mech} = \phi^i_{ECM} W^i_{ECM} + \phi^i_{NEF} W^{ILM\_i}_{NEF} \tag{16}$$

in ILM layer.

The free energy functions of the solid components (ECM, OCF and NEF) are separately described below.

2.3.1. ECM free energy

The ECM proteoglycan macromolecular network is described as an isotropic deformable solid component with a free energy W^{i}_{ECM} expressed by a Neo-Hookean form:

$$W^{i}_{ECM} = \frac{1}{2} G_{ECM} \left(\bar{I}^{i}_{1} - 3 \right) \tag{17}$$

in which G_{ECM} is the ECM shear modulus and $\bar{I}^{i}_{1} = \text{trace}\left(\mathbf{C}^{i}_{mech} \right)$ is the first stretch invariant.

2.3.2. OCF free energy

The OCF network gives anisotropy, high stiffness and mechanical resistance to annulus. The sketch in Fig. 4 shows the different stretch stages of a stretched fiber in relation to its deformation behavior. In addition to fiber orientation and intrinsic properties, the description of the OCF nonlinear response requires two distinct relations below and above a stretch λ^{*}_{OCF} to consider the deformation-induced morphological evolution. The OCF free energy W^{i}_{OCF} is expressed as a function of the fourth stretch invariant $\bar{I}^{i}_{4\theta} = \boldsymbol{a} . \mathbf{C}^{i}_{mech} . \boldsymbol{a} = \lambda^{i2}_{\theta}$ by:

$$W^{i}_{OCF} = H\left(\bar{I}^{i}_{4\theta} - 1 \right) \left[\frac{1}{2} \frac{C_1}{C_2} \left(\exp\left(C_2 \left(\bar{I}^{i}_{4\theta} - 1 \right)^2 \right) - 1 \right) \right] \quad \lambda^{i}_{\theta} < \lambda^{*}_{OCF} \tag{18}$$

below λ^{*}_{OCF} and,

$$W^{i}_{OCF} = H\left(\bar{I}^{i}_{4\theta} - 1 \right) \left[\frac{C_3}{2} \left(\bar{I}^{i}_{4\theta} - \bar{I}^{*}_{4\theta} \right)^2 + \zeta \left(\bar{I}^{i}_{4\theta} - \nu \right) \right] \quad \lambda^{i}_{\theta} \geq \lambda^{*}_{OCF} \tag{19}$$

above λ^{*}_{OCF}.

The stretch λ^{*}_{OCF} defines the stretch transition between the ‘toe’ and ‘linear’ regions of the stress-stretch curve [25, 48-49]. These two regions are related to the peculiar local behavior of a collagen fiber passing from the initially undulated configuration to the fully stretched state as illustrated in Fig. 4. The terms C_1, C_2 and C_3 are material constants of the OCF, $H(\bullet)$ is the Heaviside function that ensures only stretching of the OCF, $\bar{I}^{*}_{4\theta}$ is the fourth stretch invariant for $\lambda^{i}_{\theta} = \lambda^{*}_{OCF}$ and, ζ and ν are functions that ensure continuity between ‘toe’ and ‘linear’ regions:

$$\zeta = C_1\left(\bar{I}^*_{4\theta}-1\right)\exp\left(C_2\left(\bar{I}^*_{4\theta}-1\right)^2\right) \text{ and } \nu = \bar{I}^*_{4\theta} - \frac{C_1}{2C_2\zeta}\left(\exp\left(C_2\left(\bar{I}^*_{4\theta}-1\right)^2\right)-1\right) \quad (20)$$

2.3.3. NEF free energy

The inter-fibrillar and inter-lamellar network of fibrils is described by the free energy $W^{\ i}_{NEF}$ given by:

$$W^{LM\_i}_{NEF} = \sum_{\eta}\sum_{\psi}\phi^{LM\_i}_{\eta}W^i_{\psi} \text{ and } W^{ILM\_i}_{NEF} = \sum_{\eta=45,90,135}\sum_{\psi}\phi^{ILM\_i}_{\eta}W^i_{\psi} \quad (21)$$

For the same reasons invoked for OCF, the free energy of each fibril $W^{\ i}_{\psi}$ is given by two distinct relations below and above a stretch λ^*_{NEF}:

$$W^i_{\psi} = H\left(\bar{I}^i_{4\psi}-1\right)\left[\frac{1}{2}\frac{C_4}{C_5}\left(\exp\left(C_5\left(\bar{I}^i_{4\psi}-1\right)^2\right)-1\right)\right] \quad \lambda^i_{\psi} < \lambda^*_{NEF} \quad (22)$$

below λ^*_{NEF} and,

$$W^i_{\psi} = H\left(\bar{I}^i_{4\psi}-1\right)\left[\frac{C_6}{2}\left(\bar{I}^i_{4\psi}-\bar{I}^*_{4\psi}\right)^2 + \zeta_{\psi}\left(\bar{I}^i_{4\psi}-\nu_{\psi}\right)\right] \quad \lambda^i_{\psi} \geq \lambda^*_{NEF} \quad (23)$$

above λ^*_{NEF}.

The terms C_4, C_5 and C_6 are material constants of the NEF, $H(\bullet)$ is again the Heaviside function, $\bar{I}^i_{4\psi} = \boldsymbol{b}_{\psi}.\mathbf{C}^i_{mech}.\boldsymbol{b}_{\psi} = \lambda^{i\,2}_{\psi}$ is the fourth stretch invariant for the NEF, $\bar{I}^*_{4\psi}$ is the fourth stretch invariant for $\lambda^i_{\psi} = \lambda^*_{FCN}$ and, ζ_{ψ} and ν_{ψ} are two functions expressed as:

$$\zeta_{\psi} = C_4\left(\bar{I}^*_{4\psi}-1\right)\exp\left(C_5\left(\bar{I}^*_{4\psi}-1\right)^2\right) \text{ and } \nu_{\psi} = \bar{I}^*_{4\psi} - \frac{C_4}{2C_5\zeta_{\psi}}\left(\exp\left(C_5\left(\bar{I}^*_{4\psi}-1\right)^2\right)-1\right) \quad (24)$$

2.4. Damage

Under external mechanical loading, the nature of local failure is the scission of the ECM tangled proteoglycan macromolecules, the detachment of the internal bonds in the discrete (inter-fibrillar and inter-lamellar) fibrils and the breaking of the regularly-oriented fibers. When an individual solid component (ECM, OCF and NEF) is broken, it does no longer contribute to sustain the macro-stress. Damage induces thus a progressive evolution of the effective amount of the solid components:

$$\phi^i_{ECM\_d} = \phi^i_{ECM}\left(1-d^i_{ECM}\right),\ \phi^i_{OCF\_d} = \phi^i_{OCF}\left(1-d^i_{OCF}\right),\ \phi^i_{\eta\_d} = \phi^i_{\eta}\left(1-d^i_{\psi}\right) \quad (25)$$

where d^{i}_{ECM}, d^{i}_{OCF} and d^{i}_{ψ} characterize the damage evolution occurring within the multi-layered material element microstructure. This damage representation is in line with the general damage mechanics framework for the hyperelasticity theory. The respective internal stress of each solid component is considered as the quantity controlling the progressive damage evolution from 0.0 for the virgin state to 1.0 for the fully damaged state. Two-parameter Weibull statistical distributions are used to introduce the stochastic nature of the damage process:

$$d^{i}_{ECM} = 1 - \exp\left(-\left(\frac{\left\| \mathbf{P}^{i}_{ECM} \right\|}{\beta_{ECM}} \right)^{\alpha_{ECM}} \right) \tag{26}$$

$$d^{i}_{OCF} = 1 - \exp\left(-\left(\frac{\left\| \mathbf{P}^{i}_{OCF} \right\|}{\beta_{OCF}} \right)^{\alpha_{OCF}} \right) \tag{27}$$

$$d^{i}_{\psi} = 1 - \exp\left(-\left(\frac{\left\| \mathbf{P}^{i}_{\psi} \right\|}{\beta_{NEF}} \right)^{\alpha_{NEF}} \right) \tag{28}$$

in which α and β are two damage parameters controlling respectively the damage rate and the damage level, $\left\| \mathbf{P}^{i}_{ECM} \right\|$, $\left\| \mathbf{P}^{i}_{OCF} \right\|$ and $\left\| \mathbf{P}^{i}_{\psi} \right\|$ are the effective first Piola-Kirchhoff stresses given by the Frobenius norm:

$$\left\| \mathbf{P}^{i}_{ECM} \right\| = \sqrt{\mathrm{tr}\left(\mathbf{P}^{i}_{ECM} \mathbf{P}^{i^{T}}_{ECM} \right)}, \left\| \mathbf{P}^{i}_{OCF} \right\| = \sqrt{\mathrm{tr}\left(\mathbf{P}^{i}_{OCF} \mathbf{P}^{i^{T}}_{OCF} \right)} \text{ and } \left\| \mathbf{P}^{i}_{\psi} \right\| = \sqrt{\mathrm{tr}\left(\mathbf{P}^{i}_{\psi} \mathbf{P}^{i^{T}}_{\psi} \right)} \tag{29}$$

Taking into consideration the organization of the collagen network at different scales (as illustrated in Fig. 1) allows to propose a proper description of the progressive degradation considering both localization and anisotropy. The coupling between damage and osmotic effects is considered by introducing the following modification of the chemical-induced volumetric change:

$$\varepsilon^{i}_{chem\_d} = \varepsilon^{i}_{chem} \left(1 - d^{i}_{ECM} \right) \left(1 - d^{i}_{OCF} \right) \left(1 - d^{i}_{NEF} \right) \tag{30}$$

in which $d^{i}_{NEF} = 1/n \sum_{\psi}^{n} d^{i}_{\psi}$ is the damage of NEF and n is the number of fibrils.

2.5. Summary of the model

A new model for the microscopic description of the annulus mechanics is constructed by using the constitutive equations described above. To formulate the overall mechanical

response of the multi-layered annulus under general three-dimensional loading conditions, the compatibility at inter-layer interfaces (Fig. 2a) must be respected while the above descriptions and definitions are used. In this regard, the continuity conditions in deformation and stress to be satisfied are:

$$\mathbf{F}^{LM\_i}.\boldsymbol{n}_0^i = \mathbf{F}^{ILM\_i+1}.\boldsymbol{n}_0^i \text{ and } \boldsymbol{\sigma}^{LM\_i}.\boldsymbol{n}^i = \boldsymbol{\sigma}^{ILM\_i+1}.\boldsymbol{n}^i \tag{31}$$

where $\boldsymbol{n}_0^i$ and $\boldsymbol{n}^i$ are the arbitrary unit vectors between two adjacent layers in the initial and current configurations, respectively.

The macro-deformation $\mathbf{F}$ and the macro-stress $\boldsymbol{\sigma}$ of the soft tissue are expressed as [47]:

$$\mathbf{F} = \sum_{i=1,3...}^{m} \phi_{layer\_0}^i \mathbf{F}^{LM\_i} + \sum_{i=2,4...}^{m-1} \phi_{layer\_0}^i \mathbf{F}^{ILM\_i} \tag{32}$$

and

$$\boldsymbol{\sigma} = \sum_{i=1,3,..}^{m} \phi_{layer}^i \boldsymbol{\sigma}^{LM\_i} + \sum_{i=2,4,..}^{m-1} \phi_{layer}^i \boldsymbol{\sigma}^{ILM\_i} \tag{33}$$

where the deformation gradients and the Cauchy stresses in LM and ILM are given by their volumetric and mechanical parts:

$$\mathbf{F}^{LM\_i} = \mathbf{F}_{chem}^{LM\_i}.\mathbf{F}_{mech}^{LM\_i} \text{ and } \mathbf{F}^{ILM\_i} = \mathbf{F}_{chem}^{ILM\_i}.\mathbf{F}_{mech}^{ILM\_i} \tag{34}$$

and

$$\boldsymbol{\sigma}^{LM\_i} = \boldsymbol{\sigma}_{mech}^{LM\_i} + \boldsymbol{\sigma}_{chem}^{LM\_i} \text{ and } \boldsymbol{\sigma}^{ILM\_i} = \boldsymbol{\sigma}_{mech}^{ILM\_i} + \boldsymbol{\sigma}_{chem}^{ILM\_i} \tag{35}$$

The deformation gradients are detailed in Appendix A. The different parts of the Cauchy stress tensor are provided in Appendix B. The volume fractions in the initial and current configurations, $\phi_{layer\_0}^i$ and ϕ_{layer}^i are, respectively:

$$\phi_{layer\_0}^i = \frac{z_{layer\_0}^i}{z_{tissue}} \text{ and } \phi_{layer}^i = \frac{J_{chem}^i z_{layer\_0}^i}{\sum_{j=1}^{m} J_{chem}^j z_{layer\_0}^j} \tag{36}$$

in which $z_{layer\_0}^i$ is the initial thickness of the layer i and z_{tissue} is the tissue thickness:

$$z_{tissue} = z_{layer}^{LM} + z_{layer}^{ILM} = \sum_{i=1,3,..}^{m} z_{layer}^{LM\_i} + \sum_{i=2,4,..}^{m-1} z_{layer}^{ILM\_i} \tag{37}$$

with $z_{layer}^{LM\_i}$ $i = 1,3,...m$ and $z_{layer}^{ILM\_i}$ $i = 2,4,...m-1$ are the functions describing respectively the LM thickness and the ILM thickness:

$$z_{layer}^{LM\_i} = ai + b \text{ and } z_{layer}^{ILM\_i} = r_{ILM/LM}\left(z_{layer}^{LM\_i-1}/2 + z_{layer}^{LM\_i+1}/2\right) \tag{38}$$

where $r_{ILM/LM}$ represents the thickness ratio of the two zones and, a and b are constants calculated according to the maximum and minimum thicknesses of the annulus layers z_{max} and z_{min}:

$$a = \frac{z_{max} - z_{min}}{m-1} \text{ and } b = z_{min} - a \tag{39}$$

where m is the number of layers.

The model makes it possible to estimate the deformation-induced damage and failure of annulus under three-dimensional loading conditions. The multi-layered material element will be subjected to the different mechanical paths illustrated in Fig. 5, namely, uniaxial (UA) stretching in different directions (circumferential, radial and tilted), biaxial stretching and shearing.

3. Results and discussion

In addition to the hierarchical organization of the collagen network presented in Section 2.1, some direct structure inputs required by the modeling (namely dimensions, collagen orientation/content and water content) are extracted from well-documented papers of the literature [11, 50-53] and are listed in Table 1. The in-vitro experiments used for model identification and verification do not generally precise the exact disc region whereas variations in water content and collagen content/orientation actually exist. Due to the lack of precise information, the selected structure features are representative of the annulus anterior area. Nine LM/ILM layers are considered resulting in a parallelepipedic material element of 10 × 4 × 4 mm for circumferential direction, and 2 × 2 × 4 mm for radial direction, in order to respect the sample size effect on the mechanical behavior of the annulus [34, 54]. The simulations were performed by using a constant strain rate of 0.001 s^{-1}.

Table 2 gives the identified values of the intrinsic mechanical parameters of the solid components (ECM, OCF and NEF) and the swelling response. Their identification was solved numerically as an optimization problem using Matlab software considering the two following objective functions $F_{swelling}^{obj}$ and F_{stress}^{obj} to be minimized:

$$F_{swelling}^{obj} = \frac{1}{\rho}\sum_{h=1}^{\rho}\left(\left(\frac{\lambda_y^h - \tilde{\lambda}_y^h}{\tilde{\lambda}_y^h}\right)^2 + \left(\frac{\lambda_z^h - \tilde{\lambda}_z^h}{\tilde{\lambda}_z^h}\right)^2 + \left(\frac{\varepsilon_{chem}^h - \tilde{\varepsilon}_{chem}^h}{\tilde{\varepsilon}_{chem}^h}\right)^2\right) \tag{40}$$

$$F_{stress}^{obj} = \frac{1}{\rho}\sum_{h=1}^{\rho}\left(\left(\frac{P_{circ}^{h} - \tilde{P}_{circ}^{h}}{\tilde{P}_{circ}^{h}}\right)^2 + \left(\frac{P_{rad}^{h} - \tilde{P}_{rad}^{h}}{\tilde{P}_{rad}^{h}}\right)^2\right) \tag{41}$$

in which the letters with an overbar denote the experimental data with ρ the number of considered data points. The optimization of the model parameters was performed using a few well-known available datasets of the swelling response (transversal stretches and volumetric strain) and the UA (circumferential and radial) stress responses till moderate stretching and ultimate failure. Before their final optimization using formulae (40) and (41), a first set of model parameters was estimated via a step-by-step approach to dissociate the different phenomena: osmotic effect, directional-dependent straightening of collagen networks and damage effect. The volumetric parameters, K_1 and K_2, were identified using the UA circumferential data of Baldit [53] describing the time-dependent volumetric response upon stretching followed by relaxation. The collagen parameters, C_1, C_2, C_4 and C_5, were identified using the nonlinear part (toe zone) of the UA circumferential data of Acaroglu et al. [51] and the radial data of Fujita et al. [55]. The stretches, λ_{OCF}^{*} and λ_{FCN}^{*}, as well as the remaining collagen parameters, C_3 and C_6, were determined using the transition between the UA nonlinear response and the UA linear response of the Acaroglu et al. [51] and Fujita et al. [55] data. The OCF damage parameters, α_{OCF} and β_{OCF}, were determined using the UA circumferential data of Acaroglu et al. [51] whereas the ECM and NEF damage parameters, α_{ECM}, β_{ECM}, α_{NEF} and β_{NEF}, were determined using the UA radial data of Fujita et al. [55]. Unless explicitly otherwise stated, the values in Table 2 will be employed in all model results, especially to generate the multiaxial model predictions under other loading paths.

3.1. Chemical-induced swelling

The swelling response was identified using experimental data under free-swelling and UA circumferential stretching [51, 53]. For the latter, only moderate levels of stretching are available in the literature. The variation of fluid content by osmotic effect is firstly used to identify the free-swelling response. The identification result is provided in Fig. 6a until chemical equilibrium in a (physiological) 0.15 NaCl solution. The volumetric tissue deformation induced by the internal fluid content variation under mechanical loading was then calibrated using the experimental data of Baldit [53] considering UA circumferential stretching and relaxation at constant circumferential stretch under a NaCl concentration of the

surrounding environment of 0.15 M. The temporal changes of transversal (radial and axial) stretches and the associated circumferential stress are given in Fig. 7. Our model considers the time-dependent chemo-mechanical coupling in the soft tissue to capture the unusual transversal strain history in relation to the actual structure and the chemical-induced internal fluid variation. The strong shrinking in the axial direction and the swelling in the radial direction upon UA circumferential stretching tend towards more usual transversal behavior upon relaxation due to chemo-mechanical equilibrium. The ILM zone is introduced as the key structural parameter governing inter-lamellae fluid exchanges under external mechanical loading and especially the auxetic behavior. This annulus feature was only appreciated through very recent contributions [47, 46, 56] and was shown as determinant in the time-dependent multiaxial response [34]. The ILM anatomic function is also to confer a shearing resistance to the annulus and the inclusion of the network of inter-lamellar fibrils in the model allows a more realistic material representation. Note that the ECM reorganization may induce viscoelastic features in the annulus fibrosus [57]. Nonetheless, the quantitative estimation of the coupling between viscoelastic effects and chemical-induced volumetric effects showed that the volumetric features are first-order factors in the annulus mechanics compared to the deformation-induced viscoelastic stress in ECM [34, 46, 56]. Although the solid components are described by purely hyperelastic laws, the present constitutive representation considers the rate-dependency of the annulus mechanics implied by the deformation-induced damage mechanisms and the volumetric effects.

The results in Fig. 7 are presented for a moderate stretch range within which the soft tissue stays in a physiological level avoiding any damage effects. The question which arises is now how the tissue behaves under large strains till final failure by including as time-dependent physical process both volumetric effects and damage accumulation.

3.2. UA stretching path

The model efficiencies to capture the stress-stretch behavior of the annulus till failure under UA stretching is presented in Figs. 8 and 9 for the two main directions in comparison with the experimental data extracted from the works of Acaroglu et al. [51] and Tavakoli and Costi [57]. The numerical curves show an excellent agreement with the annulus circumferential experimental results of Acaroglu et al. [51] in Fig. 8a including the nonlinear stress-stretch response and the failure stage displaying stress drop. Fig. 8c shows that both moduli and ultimate properties are in agreement with other data taken form the literature [58]. A direct relation between the annulus circumferential mechanics and the microstructure at the different

scales can be pointed out. The straightening of the collagen network during stretching causes a (toe) nonlinear macro-response until the disappearance of the undulations of the collagen fibers at a strain of about 13%. Then, a nearly linear response appears up to reach the limiting extensibility of the collagen fibers that is seen at a strain of about 16%. A catastrophic stiffness decrease is then observed at a strain of about 18% due to damage accumulation that arises out of a wide fibril network degradation. The circumferential stretching creates ionic imbalance and chemical stress due to chemo-mechanical coupling. The predicted volumetric change is provided in Fig. 6b and is found moderately affected by the damage. Nonetheless, the chemical disorder induced by the fluid phase diffusion through the tissue plays an important role in absorbing the mechanical loads applied to the annulus.

Fig. 8b shows the progressive damage events in ECM, OCF and NEF upon a circumferential UA stretching. The figure provides a clear picture of the sequence of damage operating in the different solid components. Before the incubation stretch, from which the damage initiates, the chemo-mechanical coupling is a reversible process dependent on hydration. The critical stretch is the lowest for ECM and the highest for OCF. The progressive breaking of NEF leads to the progressive loss of connectivity between neighboring OCF in a same LM layer, but also between OCF of two neighboring LM layers. The damage in NEF during circumferential stretching can be explained by NEF stretching due to annulus chemical expansion (Fig. 6b). The latter has profound impact on the local damage events and thus on the overall annulus mechanics, especially along the circumferential direction. Without diffusion mechanism, the damage process is activated prematurely as evidenced in Fig. 8b. That results in stiffening, lower stretchability and a remarkably weakened stress peak as shown in Fig. 8a.

Fig. 9a shows the UA macro-stress response in the radial direction. A fairly good agreement between the experimental data of Tavakoli and Costi [57] and the model result is shown in Fig. 9a, and that, until complete loss of tissue integrity. Although the data of Tavakoli and Costi [57] concern bovine annulus, Fig. 9c points out that both moduli and ultimate properties of human annulus, taken from the work of Fujita et al. [55], are also well reproduced by the model using the same set of parameters. Stretching in the radial direction shows a different behavior to that exhibited in the circumferential direction. This directional effect is observed both in the stress response and in the damage mechanisms. The radial stretchability of the annulus is considerably higher than the circumferential stretchability. The maximum stress is observed at a strain of approximately 200%. Because they are load-bearing elements in the radial direction, the onset of damage is earlier in NEF than in ECM as shown in Fig. 9b. In

this direction, OCF experiences no damage. The increase in damage amount of NEF causes a decrease in stiffness until the observable peak stress at approximately 0.37 MPa. After the peak stress, both undamaged NEF and ECM continue to resist the applied stretching until the appearance of a second local peak stress at a strain of approximately 400%. Fig. 9c presents the moduli and the ultimate properties.

As shown in Fig. 10 the local stress response in fibrils differs according to the macroscopic stretching direction. In physics, the localization and concentration of the maximum stress in fibrils is highly dependent on the regional variation of the orientation of the bundles of fibrils, i.e. inter-fibrillar and inter-lamellar fibrils, respectively, in LM and ILM zones.

The model is also used to analyze the macroscopic failure behavior. The annulus is uniaxially stretched till failure along a loading direction successively tilted from the circumferential direction to the radial direction. The failure state is identified as the maximum stress corresponding to the first local failure detected. The computed ultimate points in terms of effective stress and maximum principal strain are reported in Fig. 11 such that failure envelops are formed. A global view at these plots shows a strong directional effect on the macroscopic ultimate properties due to the layered LM/ILM organization and to the anisotropic local response of the collagen network in the LM and ILM zones. The respective role of the collagen network and the chemical effect on the UA failure response is identified in Fig. 11.

A deeper understanding of the annulus mechanics till final failure is brought by our modeling approach. The NEF supports the inter-layer connection and makes the annulus stiff especially in the radial direction. As illustrated in Fig. 9a when the NEF influence is neglected in the model a weak annulus resistance is obtained in the radial direction and a single peak stress is observed. By contrast, in the circumferential direction, no significant change is pointed out in the failure response as shown in Fig. 11. Nonetheless, as the stretching direction approaches radially, the annulus becomes much softer, with low failure stresses and high failure strains.

3.3. Biaxial stretching path

The biaxiality effects on the annulus stress-stretch curves till failure are presented in Fig. 12 for different biaxial states. As far as we know, no experimental data are available in the literature when circumferential stretching and radial stretching are combined. These results are for predictive purpose only. The computed results are shown for different strain loading ratios (= circumferential strain : radial strain, {1:0, 0:1, 1:0.5, 1:1 and 1:2}). The stiffness and ultimate properties are strongly influenced by the biaxial stretch ratio with a larger effect on

the radial behavior than on the circumferential one. The radial stretchability of the annulus is considerably decreased under a biaxial stretching state. The difference in circumferential and radial behaviors is connected to the difference in how local failure occurs due to the collagen orientation.

The model takes into consideration the directional effects along with electro-chemical activity reproduced thought the volumetric effects. It can be employed to study how individual failure of the annulus components acts on the overall progressive failure under biaxial loading. The macro-stretches at failure are presented in Fig. 13 under a wide range of biaxial loading conditions such that a failure envelope is obtained. Again, the retained criterion is the nucleation of the local failure macroscopically identified by the maximum stress. The biaxial failure envelopes are normalized by their maximal stretch values. Different microstructure cases are considered and important insights are observed. When the collagen network is not considered, the failure is governed by the isotropic ECM and a symmetric failure envelope with respect to the main bisectrix is obtained. The symmetry is lost for the other cases. Both collagen network and LM/ILM organization significantly impact the ultimate properties by conferring a directional effect on the failure envelope.

Both tilted and biaxial stretching help us to better understand the chemo-mechanical-damage behavior of the annulus till failure in relation to the hierarchical organization of all discrete solid components.

3.4. Shearing path

To illustrate further the predictive capability of the model, the numerical results are compared to the annulus shearing data extracted from the literature in Figs. 14 and 15. The predicted stress-strain curve is found in acceptable agreement with the typical experimental curve of Tavakoli and Costi [57] in Fig. 14, highlighting the predictive capabilities of the model. Recall that this typical curve is taken from bovine annulus.

The numerical shear modulus is calculated in the toe and linear regions and reported in Fig. 15a. It is compared to shear values reported in other papers considering different species: Fujita et al. [59] for human, Gregory et al. [60] for porcine and Labus et al. [61] for bovine. Except Labus et al. [61], the precise annulus position is not provided. The model prediction of the toe shear modulus is found in acceptable agreement with that of the inner annulus from [61]; it is lower than the outer annulus since collagen content and layers dimensions are smaller. The Tavakoli and Costi [57] toe shear data, that is between the inner and outer values of Labus et al. [61], is underestimated by the model prediction. By contrast, the model is in

good agreement with the value of Fujita et al. [59]. The model overestimates the values of Gregory et al. [60] in the toe and linear regions. But for the shearing failure strain, it falls within the experimental standard deviation intervals of Gregory et al. [60] as shown in Fig. 15b. However, the shearing failure stress of Gregory et al. [60] is largely overestimated as shown in Fig. 15c. Although the predicted failure stress is found smaller than the Tavakoli and Costi [57] shearing data, the predicted failure strain is in excellent agreement with the experiments. Like a loading in radial stretching, the important role of NEF to keep the integrity of the inter-layer connection is shown again.

4. Concluding remarks

In the present paper, a novel human annulus multiscale model was proposed to constitutively relate the structure at different scales (tangled ECM, network of nano-sized fibrils/micro-sized fibers and multi-layered LM/ILM organization) and the multiaxial macroscopic response till failure in connection to volumetric effects and damage mechanisms. It was shown that the model captures quantitatively experimental observations including directional effects upon different loading histories. The model provides a useful tool for annulus failure estimate in relation to complex interactions between external loading mode, structure features, damage events and hydration.

For future works, the annulus regional microstructure will be implemented in an axisymmetric version of the present (multiscale and multiaxial) model in the main goal to predict anisotropic damage and failure in a complete intervertebral disc model including nucleus-annulus interaction.

Appendix A. Deformation gradients

A.1. Chemical-induced swelling

The hydration effect is considered in our modeling approach. Under a free-swelling, the deformation gradients of a layer *i* are:

$$\begin{aligned} \mathbf{F}^i_{mech} &= \mathbf{I} \\ \mathbf{F}^i_{chem} &= \mathrm{diag}\left(\lambda^i_{chem\_x}, \lambda^i_{chem\_y}, \lambda^i_{chem\_z}\right) \quad i = 1,2,...m \end{aligned} \tag{A1}$$

in which $\lambda^i_{chem\_x}$, $\lambda^i_{chem\_y}$ and $\lambda^i_{chem\_z}$ are the chemical stretches in the $\boldsymbol{x}$, $\boldsymbol{y}$ and $\boldsymbol{z}$ directions, respectively.

No fluid transfer occurs under shearing, i.e., $\mathbf{F}^i_{chem} = \mathbf{I}$. Under UA or biaxial stretching, the chemical deformation gradient is empirically expressed as follows:

$$\mathbf{F}_{chem}^{i}=\mathbf{I}+\mathrm{diag}\left(\xi_{x}^{i}\chi_{x}^{i}\cos\omega,\ \xi_{y}^{i}\chi_{y}^{i}\cos\omega,\ \xi_{z}^{i}\chi_{z}^{i}\right) \tag{A2}$$

Such that the chemical-induced volumetric strain ε_{chem}^{i} is given by:

$$\varepsilon_{chem}^{i}=\left(1+\xi_{x}^{i}\chi_{x}^{i}\cos\omega\right)\left(1+\xi_{y}^{i}\chi_{y}^{i}\cos\omega\right)\left(1+\xi_{z}^{i}\chi_{z}^{i}\right)-1 \tag{A3}$$

where ω is a coefficient that changes according to the loading mode.

Guided by the experimental observations of Baldit [53] and Derrouiche et al. [45] on circumferentially stretched annulus specimens, the chemical deformation gradient (A2) was initially proposed by Tamoud et al. [47]. The term ω is introduced here to consider the loading angle effect on tilted stretching behavior and on biaxial stretching behavior.

For tilted stretching, the term ω is given by:

$$\omega=\gamma \tag{A4}$$

in which γ is the angle between the loading direction and the circumferential direction.

For biaxial stretching, the term ω is geometrically deduced from the biaxiality ratio:

$$\omega=\tan^{-1}\left(\left(\lambda_{rad}-1\right)/\left(\lambda_{circ}-1\right)\right) \tag{A5}$$

in which λ_{circ} and λ_{rad} are the applied stretches in the circumferential and radial directions, respectively.

The terms ξ_{x}^{i}, ξ_{y}^{i} and ξ_{z}^{i} are the chemical expansions at the equilibrium state and, χ_{x}^{i}, χ_{y}^{i} and χ_{z}^{i} are functions of time [47]:

$$\chi_{x}^{i}=1-\exp\left(-t/\tau_{x}^{i}\right),\ \chi_{y}^{i}=1-\exp\left(-t/\tau_{y}^{i}\right)\ \text{and}\ \chi_{z}^{i}=1-\exp\left(-t/\tau_{z}^{i}\right) \tag{A6}$$

where τ_{x}^{i}, τ_{y}^{i} and τ_{z}^{i} are the chemical expansion rates.

In what follows, the mechanical deformation gradients of each loading case, given in Fig. 5, are separately provided.

A.2. UA stretching path

The UA stretching of the multi-layered material element can be carried out along the circumferential direction, along the radial direction or along a direction tilted by an angle γ with respect to the circumferential direction. The mechanical deformation gradients may be expressed as a function of the applied stretch λ and the stretch in the fiber direction λ_{f} :

$$\mathbf{F}_{mech}^{LM\_i}=\mathbf{R}_{y}^{\gamma}.\left[\mathbf{R}_{z}^{\theta\_i}.\mathrm{diag}\left(\lambda_{f},\lambda_{f}^{-1/2},\lambda_{f}^{-1/2}\right).\mathbf{R}_{z}^{\theta\_i^{T}}\right].\mathbf{R}_{y}^{\gamma^{T}}\quad i=1,3,...m \tag{A7}$$

in LM layer and,

$$\mathbf{F}_{mech}^{ILM\_i} = \mathbf{R}_y^{\gamma}.\mathrm{diag}\left(\frac{\lambda}{\lambda_{chem\_x}^i}, \left(\frac{\lambda}{\lambda_{chem\_x}^i}\right)^{-1/2}, \left(\frac{\lambda}{\lambda_{chem\_x}^i}\right)^{-1/2}\right).\mathbf{R}_y^{\gamma^T} \quad i = 2,4,...m-1 \tag{A8}$$

in ILM layer.

The quantities $\mathbf{R}_z^{\theta\_i}$ and $\mathbf{R}_y^{\gamma}$ are the basis-change tensor in each layer, with a rotation θ^i around the ***z***-axis and stretch direction γ around the ***y***-axis, respectively:

$$\mathbf{R}_z^{\theta\_i} = \begin{bmatrix} \cos\theta^i & \sin\theta^i & 0 \\ -\sin\theta^i & \cos\theta^i & 0 \\ 0 & 0 & 1 \end{bmatrix} \text{ and } \mathbf{R}_y^{\gamma} = \begin{bmatrix} \cos\gamma & 0 & -\sin\gamma \\ 0 & 1 & 0 \\ \sin\gamma & 0 & \cos\gamma \end{bmatrix} \tag{A9}$$

After a series of lengthy but straightforward derivations, we get the mechanical deformation gradients under UA stretching path:

$$\mathbf{F}_{mech}^{LM\_i} = \begin{bmatrix} \frac{\lambda\cos^2\gamma}{\lambda_{chem\_x}^i} + \frac{\sin^2\gamma}{\sqrt{S_2^i}} & S_3^i\cos\gamma & \cos\gamma\sin\gamma\left(\frac{\lambda}{\lambda_{chem\_x}^i} - \frac{1}{\sqrt{S_2^i}}\right) \\ S_3^i\cos\gamma & \frac{\lambda_{chem\_x}^i}{\lambda}\left(\sqrt{S_2^i} + S_3^{i\,2}\right) & S_3^i\sin\gamma \\ \cos\gamma\sin\gamma\left(\frac{\lambda}{\lambda_{chem\_x}^i} - \frac{1}{\sqrt{S_2^i}}\right) & S_3^i\sin\gamma & \frac{\lambda\sin^2\gamma}{\lambda_{chem\_x}^i} + \frac{\cos^2\gamma}{\sqrt{S_2^i}} \end{bmatrix} \tag{A10}$$

in LM layer and,

$$\mathbf{F}_{mech}^{ILM\_i} = \begin{bmatrix} \frac{\lambda\cos^2\gamma}{\lambda_{chem\_x}^i} + \frac{\sin^2\gamma}{\sqrt{\frac{\lambda}{\lambda_{chem\_x}^i}}} & 0 & \cos\gamma\sin\gamma\left(\frac{\lambda}{\lambda_{chem\_x}^i} - \frac{1}{\sqrt{\frac{\lambda}{\lambda_{chem\_x}^i}}}\right) \\ 0 & \frac{1}{\sqrt{\frac{\lambda}{\lambda_{chem\_x}^i}}} & 0 \\ \cos\gamma\sin\gamma\left(\frac{\lambda}{\lambda_{chem\_x}^i} - \frac{1}{\sqrt{\frac{\lambda}{\lambda_{chem\_x}^i}}}\right) & 0 & \frac{\lambda\sin^2\gamma}{\lambda_{chem\_x}^i} + \frac{\cos^2\gamma}{\sqrt{\frac{\lambda}{\lambda_{chem\_x}^i}}} \end{bmatrix} \tag{A11}$$

in ILM layer.

The terms S_1^i, S_2^i and S_3^i are given by:

$$S_1^i = \left(\sqrt{\frac{\tan^4\theta^i}{4} - \left(\frac{\lambda}{\lambda_{chem\_x}^i} \frac{1}{3\cos^2\theta^i} \right)^3} - \frac{\tan^2\theta^i}{2} \right)^{1/3}$$

$$S_2^i = \left(S_1^i + \frac{\lambda}{\lambda_{chem\_x}^i} \frac{1}{3S_1^i \cos^2\theta^i} \right)^2 \tag{A12}$$

$$S_3^i = \cos\theta^i \sin\theta^i \left(S_2^i - \frac{1}{\sqrt{S_2^i}} \right)$$

A.3. Biaxial stretching path

The biaxial mechanical deformation gradients may be expressed as a function of the stretches in the fiber axes $\lambda_{f_{x_1}}$, $\lambda_{f_{x_2}}$ and $\lambda_{f_{x_3}}$:

$$\mathbf{F}_{mech}^{LM\_i} = \mathbf{R}_z^{\theta\_i} . \mathrm{diag}\left(\lambda_{f_{x_1}}, \lambda_{f_{x_2}}, \lambda_{f_{x_3}} \right) . \mathbf{R}_z^{\theta\_i^T} \quad i = 1,3,...m \tag{A13}$$

in LM layer and,

$$\mathbf{F}_{mech}^{ILM\_i} = \mathrm{diag}\left(\frac{\lambda_{circ}}{\lambda_{chem\_x}^i}, \frac{\lambda_{chem\_x}^i \lambda_{chem\_z}^i}{\lambda_{circ}\lambda_{rad}}, \frac{\lambda_{rad}}{\lambda_{chem\_z}^i} \right) \quad i = 2,4,...m-1 \tag{A14}$$

in ILM layer.

The mechanical deformation gradient in LM layer is given by:

$$\mathbf{F}_{mech}^{LM\_i} = \begin{bmatrix} \frac{\lambda_{circ}}{\lambda_{chem\_x}^i} & S_6^i & 0 \\ S_6^i & S_5^i & 0 \\ 0 & 0 & \frac{\lambda_{rad}}{\lambda_{chem\_z}^i} \end{bmatrix} \tag{A15}$$

The terms S_4^i, S_5^i and S_6^i are given by:

$$S_4^i = \frac{\lambda_{circ}}{\lambda_{chem\_x}^i} - \sqrt{\left(\frac{\lambda_{cir}}{\lambda_{chem\_x}^i} \right)^2 - \frac{\lambda_{chem\_z}^i \left(2\cos\theta^i \sin\theta^i \right)^2}{\lambda_{rad}}}$$

$$S_5^i = \tan^2\theta^i \left(\frac{\lambda_{circ}}{\lambda_{chem\_x}^i} + \frac{S_4^i \left(\tan^{-4} - 1 \right)}{2} \right) \tag{A16}$$

$$S_6^i = \frac{\lambda_{circ} \tan\theta^i}{\lambda_{chem\_x}^i} - \frac{S_4^i}{2\cos\theta^i \sin\theta^i}$$

A.4. Shearing path

The annulus under shearing is subjected to the following mechanical deformation gradients:

$$\mathbf{F}_{mech}^{LM\_i} = \mathbf{F}_{mech}^{ILM\_i} = \begin{bmatrix} 1 & 0 & 0 \\ 0 & 1 & \kappa \\ 0 & \kappa & 1 \end{bmatrix} \tag{A17}$$

where κ is the shear stretch.

Appendix B. Multi-layered annulus behavior

The mechanical Cauchy stress tensor $\boldsymbol{\sigma}_{mech}^{i}$ is written as follows:

$$\boldsymbol{\sigma}_{mech}^{LM\_i} = \boldsymbol{\sigma}_{ECM}^{i} + \boldsymbol{\sigma}_{OCF}^{LM\_i} + \boldsymbol{\sigma}_{NEF}^{LM\_i} \tag{B1}$$

in LM layer and,

$$\boldsymbol{\sigma}_{mech}^{ILM\_i} = \boldsymbol{\sigma}_{ECM}^{i} + \boldsymbol{\sigma}_{NEF}^{ILM\_i} \tag{B2}$$

in ILM layer.

The NEF Cauchy stress tensor $\boldsymbol{\sigma}_{NEF}^{i}$ is given by the sum of the Cauchy stress tensor $\boldsymbol{\sigma}_{NEF_{\psi}^{\eta}}^{i}$ of all discrete fibrils as follows:

$$\boldsymbol{\sigma}_{NEF}^{LM\_i} = \sum_{\eta}\sum_{\psi} \boldsymbol{\sigma}_{NEF_{\psi}^{\eta}}^{LM\_i} \text{ and } \boldsymbol{\sigma}_{NEF}^{ILM\_i} = \sum_{\eta=45,90,135}\sum_{\psi} \boldsymbol{\sigma}_{NEF_{\psi}^{\eta}}^{ILM\_i} \tag{B3}$$

In Eq. (14), the derivation may be expressed as follows:

$$\frac{\partial W_{mech}^{i}}{\partial \mathbf{C}_{mech}^{i}} = \frac{\partial W_{mech}^{i}}{\partial \bar{I}_{1}^{i}} \frac{\partial \bar{I}_{1}^{i}}{\partial \mathbf{C}_{mech}^{i}} + \frac{\partial W_{mech}^{i}}{\partial \bar{I}_{4\theta}^{i}} \frac{\partial \bar{I}_{4\theta}^{i}}{\partial \mathbf{C}_{mech}^{i}} + \frac{\partial W_{mech}^{i}}{\partial \bar{I}_{4\psi}^{i}} \frac{\partial \bar{I}_{4\psi}^{i}}{\partial \mathbf{C}_{mech}^{i}} \tag{B4}$$

with

$$\frac{\partial \bar{I}_{1}^{i}}{\partial \mathbf{C}_{mech}^{i}} = \mathbf{I}, \quad \frac{\partial \bar{I}_{4\theta}^{i}}{\partial \mathbf{C}_{mech}^{i}} = \boldsymbol{a} \otimes \boldsymbol{a} \text{ and } \frac{\partial \bar{I}_{4\psi}^{i}}{\partial \mathbf{C}_{mech}^{i}} = \boldsymbol{b}_{\psi} \otimes \boldsymbol{b}_{\psi} \tag{B5}$$

After a series of straightforward derivations, the different parts of the Cauchy stress tensor are given by:

$$\boldsymbol{\sigma}_{ECM}^{i} = \phi_{ECM\_d}^{i} G_{ECM} \mathbf{F}_{mech}^{i} . \mathbf{F}_{mech}^{i^{T}} - p^{i}\mathbf{I} \tag{B6}$$

$$\begin{aligned} \boldsymbol{\sigma}_{OCF}^{LM\_i} &= H\left(\bar{I}_{4\theta}^{i} - 1\right)\left[2\phi_{OCF\_d}^{i}\left(C_1\left(\bar{I}_{4\theta}^{i} - 1\right)\exp\left(C_2\left(\bar{I}_{4\theta}^{i} - 1\right)^{2}\right)\right)\right]\mathbf{F}_{mech}^{i} . (\boldsymbol{a} \otimes \boldsymbol{a}) . \mathbf{F}_{mech}^{i^{T}} \quad \lambda_{OCF}^{i} < \lambda_{OCF}^{*} \\ \boldsymbol{\sigma}_{OCF}^{LM\_i} &= H\left(\bar{I}_{4\theta}^{i} - 1\right)\left[2\phi_{OCF\_d}^{i}\left(C_3\left(\bar{I}_{4\theta}^{i} - \bar{I}_{4\theta}^{*}\right) + \zeta\right)\right]\mathbf{F}_{mech}^{i} . (\boldsymbol{a} \otimes \boldsymbol{a}) . \mathbf{F}_{mech}^{i^{T}} \quad \lambda_{OCF}^{i} \geq \lambda_{OCF}^{*} \end{aligned} \tag{B7}$$

$$\begin{aligned} \boldsymbol{\sigma}_{NEF_{\psi}^{\eta}}^{LM\_i} &= H\left(\bar{I}_{4\psi}^{i} - 1\right)\left[2\phi_{NEF}^{i}\phi_{\eta\_d}^{LM\_i}\left(C_4\left(\bar{I}_{4\psi}^{i} - 1\right)\exp\left(C_5\left(\bar{I}_{4\psi}^{i} - 1\right)^{2}\right)\right)\right]\mathbf{F}_{mech}^{i} . (\boldsymbol{b}_{\psi} \otimes \boldsymbol{b}_{\psi}) . \mathbf{F}_{mech}^{i^{T}} \quad \lambda_{\psi}^{i} < \lambda_{NEF}^{*} \\ \boldsymbol{\sigma}_{NEF_{\psi}^{\eta}}^{LM\_i} &= H\left(\bar{I}_{4\psi}^{i} - 1\right)\left[2\phi_{NEF}^{i}\phi_{\eta\_d}^{LM\_i}\left(C_6\left(\bar{I}_{4\psi}^{i} - \bar{I}_{4\psi}^{*}\right) + \zeta_{\psi}\right)\right]\mathbf{F}_{mech}^{i} . (\boldsymbol{b}_{\psi} \otimes \boldsymbol{b}_{\psi}) . \mathbf{F}_{mech}^{i^{T}} \quad \lambda_{\psi}^{i} \geq \lambda_{NEF}^{*} \end{aligned} \tag{B8}$$

$$\boldsymbol{\sigma}_{NEF_\psi^\eta}^{ILM\_i} = H\left(\bar{I}_{4\psi}^i - 1\right)\left[2\phi_{NEF}^i \phi_{\eta\_d}^{ILM\_i}\left(C_4\left(\bar{I}_{4\psi}^i - 1\right)\exp\left(C_5\left(\bar{I}_{4\psi}^i - 1\right)^2\right)\right)\right]\mathbf{F}_{mech}^i.\left(\boldsymbol{b}_\psi \otimes \boldsymbol{b}_\psi\right).\mathbf{F}_{mech}^{i^T} \quad \lambda_\psi^i < \lambda_{NEF}^* \tag{B9}$$

$$\boldsymbol{\sigma}_{NEF_\psi^\eta}^{ILM\_i} = H\left(\bar{I}_{4\psi}^i - 1\right)\left[2\phi_{NEF}^i \phi_{\eta\_d}^{ILM\_i}\left(C_6\left(\bar{I}_{4\psi}^i - \bar{I}_{4\psi}^*\right) + \zeta_\psi\right)\right]\mathbf{F}_{mech}^i.\left(\boldsymbol{b}_\psi \otimes \boldsymbol{b}_\psi\right).\mathbf{F}_{mech}^{i^T} \quad \lambda_\psi^i \geq \lambda_{NEF}^*$$

$$\boldsymbol{\sigma}_{chem}^i = \phi_{fluid}^i K_1 \boldsymbol{\varepsilon}_{chem\_d}^i \exp\left(K_2 \boldsymbol{\varepsilon}_{chem\_d}^{i^2}\right)\mathbf{I} \tag{B10}$$

where p^i is written from boundary conditions in each loading case:

$$p^{LM\_i} = \phi_{ECM\_d}^i G_{ECM}\left[\left(\frac{\lambda_{chem\_x}^i}{\lambda}\left(\sqrt{S_2^i} + S_3^{i\,2}\right)\right)^2 + S_3^{i\,2}\right] \text{ and } p^{ILM\_i} = \phi_{ECM\_d}^i G_{ECM}\left(\frac{\lambda_{chem\_x}^i}{\lambda}\right)^2 \tag{B11}$$

for UA stretching path,

$$p^{LM\_i} = \phi_{ECM\_d}^i G_{ECM}\left(S_5^{i\,2} + S_6^{i\,2}\right) \text{ and } p^{ILM\_i} = \phi_{ECM\_d}^i G_{ECM}\left(\frac{\lambda_{chem\_x}^i \lambda_{chem\_z}^i}{\lambda_{circ}\lambda_{rad}}\right)^2 \tag{B12}$$

for biaxial stretching path and,

$$p^i = \phi_{ECM\_d}^i G_{ECM}\left(\kappa^2 + 1\right) \tag{B13}$$

for shearing path.

Acknowledgements

This work was financially supported by the PROFAS B+ Scholarships Program and the International Mobility Grants Program of the University of Lille.

References

[1] Yu, J., Peter, C., Roberts, S., Urban, J.P., 2002. Elastic fibre organization in the intervertebral discs of the bovine tail. Journal of Anatomy 201, 465-475.

[2] Pezowicz, C.A., Robertson, P.A., Broom, N.D., 2006. The structural basis of interlamellar cohesion in the intervertebral disc wall. Journal of Anatomy 208, 317-330.

[3] Pezowicz, C.A., Schechtman, H., Robertson, P.A., Broom, N.D., 2006. Mechanisms of anular failure resulting from excessive intradiscal pressure: a microstructural-micromechanical investigation. Spine 31, 2891-2903.

[4] Melrose, J., Smith, S.M., Appleyard, R.C., Little, C.B., 2008. Aggrecan, versican and type VI collagen are components of annular translamellar crossbridges in the intervertebral disc. European Spine Journal 17, 314-324.

[5] Schollum, M.L., Robertson, P.A., Broom, N.D., 2008. ISSLS prize winner: microstructure and mechanical disruption of the lumbar disc annulus: part I: a microscopic investigation of the translamellar bridging network. Spine 33, 2702-2710.

[6] Han, W.M., Nerurkar, N.L., Smith, L.J., Jacobs, N.T., Mauck, R.L., Elliott, D.M., 2012. Multi-scale structural and tensile mechanical response of annulus fibrosus to osmotic loading. Annals of Biomedical Engineering 40, 1610-1621.

[7] Yu, J., Schollum, M.L., Wade, K.R., Broom, N.D., Urban, J.P., 2015. A detailed examination of the elastic network leads to a new understanding of annulus fibrosus organization. Spine 40, 1149-1157.
[8] Vergari, C., Mansfield, J., Meakin, J.R., Winlove, P.C., 2016. Lamellar and fibre bundle mechanics of the annulus fibrosus in bovine intervertebral disc. Acta Biomaterialia 37, 14-20.
[9] Han, S.K., Chen, C.W., Labus, K.M., Puttlitz, C.M., Chen, Y., Hsieh, A.H., 2016. Optical coherence tomographic elastography reveals mesoscale shear strain inhomogeneities in the annulus fibrosus. Spine 41, 770-777.
[10] Tavakoli, J., Elliott, D.M., Costi, J.J., 2016. Structure and mechanical function of the inter-lamellar matrix of the annulus fibrosus in the disc. Journal of Orthopaedic Research 34, 1307-1315.
[11] Tavakoli, J., Elliott, D.M., Costi, J.J., 2017. The ultra-structural organization of the elastic network in the intra-and inter-lamellar matrix of the intervertebral disc. Acta Biomaterialia 58, 269-277.
[12] Tavakoli, J., Diwan, A.D., Tipper, J.L., 2020. The ultrastructural organization of elastic fibers at the interface of the nucleus and annulus of the intervertebral disk. Acta Biomaterialia 114, 323-332.
[13] Tavakoli, J., Diwan, A.D., Tipper, J.L., 2020. Elastic fibers: the missing key to improve engineering concepts for reconstruction of the nucleus pulposus in the intervertebral disc. Acta Biomaterialia 113, 407-416.
[14] Tang, H., Buehler, M.J., Moran, B., 2009. A constitutive model of soft tissue: from nanoscale collagen to tissue continuum. Annals of Biomedical Engineering 37, 1117-1130.
[15] Werbner, B., Spack, K., O'Connell, G.D., 2019. Bovine annulus fibrosus hydration affects rate-dependent failure mechanics in tension. Journal of Biomechanics 89, 34-39.
[16] Osti, O.L., Vernon-Roberts, B., Moore, R., Fraser, R.D., 1992. Annular tears and disc degeneration in the lumbar spine: a post-mortem study of 135 discs. The Journal of Bone and Joint Surgery 74, 678-682.
[17] Vernon-Roberts, B., Moore, R.J., Fraser, R.D., 2007. The natural history of age-related disc degeneration: the pathology and sequelae of tears. Spine 32, 2797-2804.
[18] Rodriguez, J.F., Cacho, F., Bea, J.A., Doblaré, M., 2006. A stochastic-structurally based three dimensional finite-strain damage model for fibrous soft tissue. Journal of the Mechanics and Physics of Solids 54, 864-886.
[19] Calvo, B., Pena, E., Martinez, M.A., Doblare, M., 2007. An uncoupled directional damage model for fibred biological soft tissues. Formulation and computational aspects. International Journal for Numerical Methods in Engineering 69, 2036-2057.
[20] Pena, E., Alastrue, V., Laborda, A., Martínez, M.A., Doblare, M., 2010. A constitutive formulation of vascular tissue mechanics including viscoelasticity and softening behaviour. Journal of Biomechanics 43, 984-989.
[21] Blanco, S., Polindara, C.A., Goicolea, J.M., 2015. A regularised continuum damage model based on the mesoscopic scale for soft tissue. International Journal of Solids and Structures 58, 20-33.
[22] Shahraki, N.M., Fatemi, A., Agarwal, A., 2015. Failure Criteria for Prediction of Clinically Relevant Damage of Annulus Fibrosus. Spine Research 1, 1-7.
[23] Li, W., 2016. Damage models for soft tissues: a survey. Journal of Medical and Biological Engineering 36, 285-307.
[24] Holzapfel, G.A., Fereidoonnezhad, B., 2017. Modeling of damage in soft biological tissues. In Biomechanics of Living Organs 5, 101-123.

[25] Li, K., Holzapfel, G.A., 2019. Multiscale modeling of fiber recruitment and damage with a discrete fiber dispersion method. Journal of the Mechanics and Physics of Solids 126, 226-244.
[26] Ghezelbash, F., Shirazi-Adl, A., Baghani, M., Eskandari, A.H., 2020a. On the modeling of human intervertebral disc annulus fibrosus: elastic, permanent deformation and failure responses. Journal of Biomechanics 102, 109463.
[27] Volokh, K.Y., 2007. Hyperelasticity with softening for modeling materials failure. Journal of the Mechanics and Physics of Solids 55, 2237-2264.
[28] Volokh, K.Y., 2011. Modeling failure of soft anisotropic materials with application to arteries. Journal of the Mechanical Behavior of Biomedical Materials 4, 1582-1594.
[29] Ghezelbash, F., Eskandari, A.H., Shirazi-Adl, A., Kazempour, M., Tavakoli, J., Baghani, M., Costi, J.J., 2020b. Modeling of human intervertebral disc annulus fibrosus with complex multi-fiber networks. Acta Biomaterialia 123, 208-221.
[30] Derrouiche, A., Zaouali, A., Zaïri, F., Ismail, J., Chaabane, M., Qu, Z., Zaïri, F., 2019. Osmo-inelastic response of the intervertebral disc. Proceedings of the Institution of Mechanical Engineers. Part H: Journal of Engineering in Medicine 233, 332-341.
[31] Derrouiche, A., Feki, F., Zaïri, F., Taktak, R., Moulart, M., Qu, Z., Ismail, J., Charfi, S., Haddar, N., Zaïri, F., 2020. How pre-strain affects the chemo-torsional response of the intervertebral disc. Clinical Biomechanics 76, 105020.
[32] Yang, B., O'Connell, G.D., 2019. Intervertebral disc swelling maintains strain homeostasis throughout the annulus fibrosus: a finite element analysis of healthy and degenerated discs. Acta Biomaterialia, 100, 61-74.
[33] Feki, F., Taktak, R., Kandil, K., Derrouiche, A., Moulart, M., Haddar, N., Zaïri, F., Zaïri, F., 2020. How osmoviscoelastic coupling affects recovery of cyclically compressed intervertebral disc. Spine 45, 160553.
[34] Kandil, K., Zaïri, F., Messager, T., Zaïri, F., 2020. Interlamellar matrix governs human annulus fibrosus multiaxial behavior. Scientific Reports 10, 19292.
[35] Kiani, C., Chen, L., Wu, Y.J., Yee, A.J., Yang, B.B., 2002. Structure and function of aggrecan. Cell Research 12, 19-32.
[36] Urban, J.P., Roberts, S., 2003. Degeneration of the intervertebral disc. Arthritis Research and Therapy 5, 120-130.
[37] Iatridis, J.C., Godburn, K., Wuertz, K., Alini, M., Roughley, P.J., 2011. Region-dependent aggrecan degradation patterns in the rat intervertebral disc are affected by mechanical loading in vivo. Spine 36, 203-209.
[38] Iatridis, J.C., MacLean, J.J., Roughley, P.J., Alini, M., 2006. Effects of mechanical loading on intervertebral disc metabolism in vivo. The Journal of Bone and Joint Surgery 88, 41-46.
[39] Vergari, C., Mansfield, J.C., Chan, D., Clarke, A., Meakin, J.R., Winlove, P.C., 2017. The effects of needle damage on annulus fibrosus micromechanics. Acta Biomaterialia 63, 274-282.
[40] Boos, N., Weissbach, S., Rohrbach, H., Weiler, C., Spratt, K.F., Nerlich, A.G., 2002. Classification of age-related changes in lumbar intervertebral discs. Spine 27, 2631-2644.
[41] Sharabi, M., Wade, K., Haj-Ali, R., 2018. The mechanical role of collagen fibers in the intervertebral disc. In Biomechanics of the Spine 7, 105-123.
[42] Sarkadi, B., Parker, J.C., 1991. Activation of ion transport pathways by changes in cell volume. Biochimica et Biophysica Acta-Reviews on Biomembranes 1071, 407-427.
[43] Guizouarn, H., Motais, R., 1999. Swelling activation of transport pathways in erythrocytes: effects of Cl−, ionic strength, and volume changes. American Journal of Physiology-Cell Physiology 276, 210-220.

[44] de los Heros, P., Pacheco-Alvarez, D., Gamba, G., 2018. Role of WNK kinases in the modulation of cell volume. In Current Topics in Membranes 81, 207-235.
[45] Derrouiche, A., Karoui, A., Zaïri, F., Ismail, J., Qu, Z., Chaabane, M., Zaïri, F., 2020. The two Poisson's ratios in annulus fibrosus: relation with the osmo-inelastic features. Mechanics of Soft Materials 2, 1.
[46] Derrouiche, A., Zaïri, F., Zaïri, F., 2019. A chemo-mechanical model for osmo-inelastic effects in the annulus fibrosus. Biomechanics and Modeling in Mechanobiology 18, 1773-1790.
[47] Tamoud, A., Zaïri, F., Mesbah, A., Zaïri, F., 2021. A microstructure-based model for time-dependent mechanics of multi-layered soft tissues and its application to intervertebral disc annulus. Meccanica 56, 585-606.
[48] Quapp, K.M., Weiss, J.A., 1998. Material characterization of human medial collateral ligament. Journal of Biomechanical Engineering 120, 757-763.
[49] Werbner, B., Zhou, M., O'Connell, G., 2017. A novel method for repeatable failure testing of annulus fibrosus. Journal of Biomechanical Engineering 139, 1-7.
[50] Skaggs, D.L., Weidenbaum, M., Iatridis, J.C., Ratcliffe, A., Mow, V.C., 1994. Regional variation in tensile properties and biochemical composition of the human lumbar anulus fibrosus. Spine, 19, 1310-1319.
[51] Acaroglu, E.R., Iatridis, J.C., Setton, L.A., Foster, R.J., Mow, V.C., Weidenbaum, M., 1995. Degeneration and aging affect the tensile behavior of human lumbar anulus fibrosus. Spine 20, 2690-2701.
[52] Holzapfel, G.A., Schulze-Bauer, C.A.J., Feigl, G., Regitnig, P., 2005. Single lamellar mechanics of the human lumbar anulus fibrosus. Biomechanics and Modeling in Mechanobiology 3, 125-140.
[53] Baldit, A., 2013. Etude des interactions hydro-chimio-mécaniques dans les tissus biologiques: application à la nutrition du disque intervertébral. Phd Thesis, University of Montpellier.
[54] Zhou, M., Bezci, S.E., O'Connell, G.D., 2019. Multiscale composite model of fiber-reinforced tissues with direct representation of sub-tissue properties. Biomechanics and Modeling in Mechanobiology 19, 745-759.
[55] Fujita, Y., Duncan, N.A., Lotz, J.C., 1997. Radial tensile properties of the lumbar annulus fibrosus are site and degeneration dependent. Journal of Orthopaedic Research 15, 814-819.
[56] Kandil, K., Zaïri, F., Derrouiche, A., Messager, T., Zaïri, F., 2019. Interlamellar-induced time-dependent response of intervertebral disc annulus: a microstructure-based chemo-viscoelastic model. Acta Biomaterialia 200, 75-91.
[57] Tavakoli, J., Costi, J.J., 2018. New findings confirm the viscoelastic behaviour of the inter-lamellar matrix of the disc annulus fibrosus in radial and circumferential directions of loading. Acta Biomaterialia 71, 411-419.
[58] Ebara, S., Iatridis, J.C., Setton, L.A., Foster, R.J., Mow, V.C., Weidenbaum, M., 1996. Tensile properties of nondegenerate human lumbar anulus fibrosus. Spine 21, 452-461.
[59] Fujita, Y., Wagner, D.R., Biviji, A.A., Duncan, N.A., Lotz, J.C., 2000. Anisotropic shear behavior of the annulus fibrosus: effect of harvest site and tissue prestrain. Medical Engineering and Physics 22, 349-357.
[60] Gregory, D.E., Veldhuis, J.H., Horst, C., Brodland, G.W., Callaghan, J.P., 2011. Novel lap test determines the mechanics of delamination between annular lamellae of the intervertebral disc. Journal of Biomechanics 44, 97-102.
[61] Labus, K.M., Han, S.K., Hsieh, A.H., Puttlitz, C. M., 2014. A computational model to describe the regional interlamellar shear of the annulus fibrosus. Journal of Biomechanical Engineering 136, 0510091.

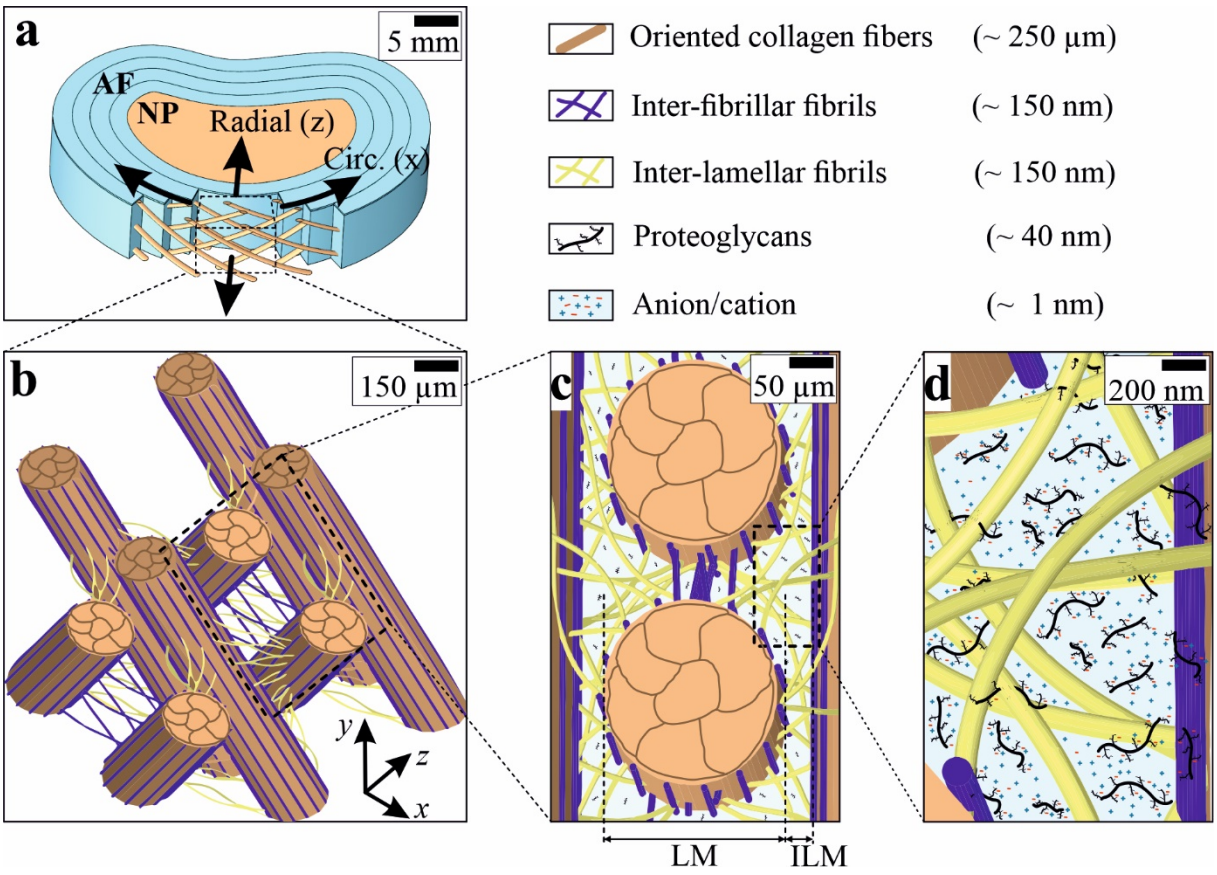

Figure 1. Multiscale view of (a) the intervertebral disc annulus fibrosus (AF: annulus fibrosus, NP: nucleus pulposus) starting from (b) the multi-layered material element to the local organization of the collagen-network at the (c) microscale and the (d) nanoscale. The picture is adapted from the experimental analyzes in [6, 7, 11].

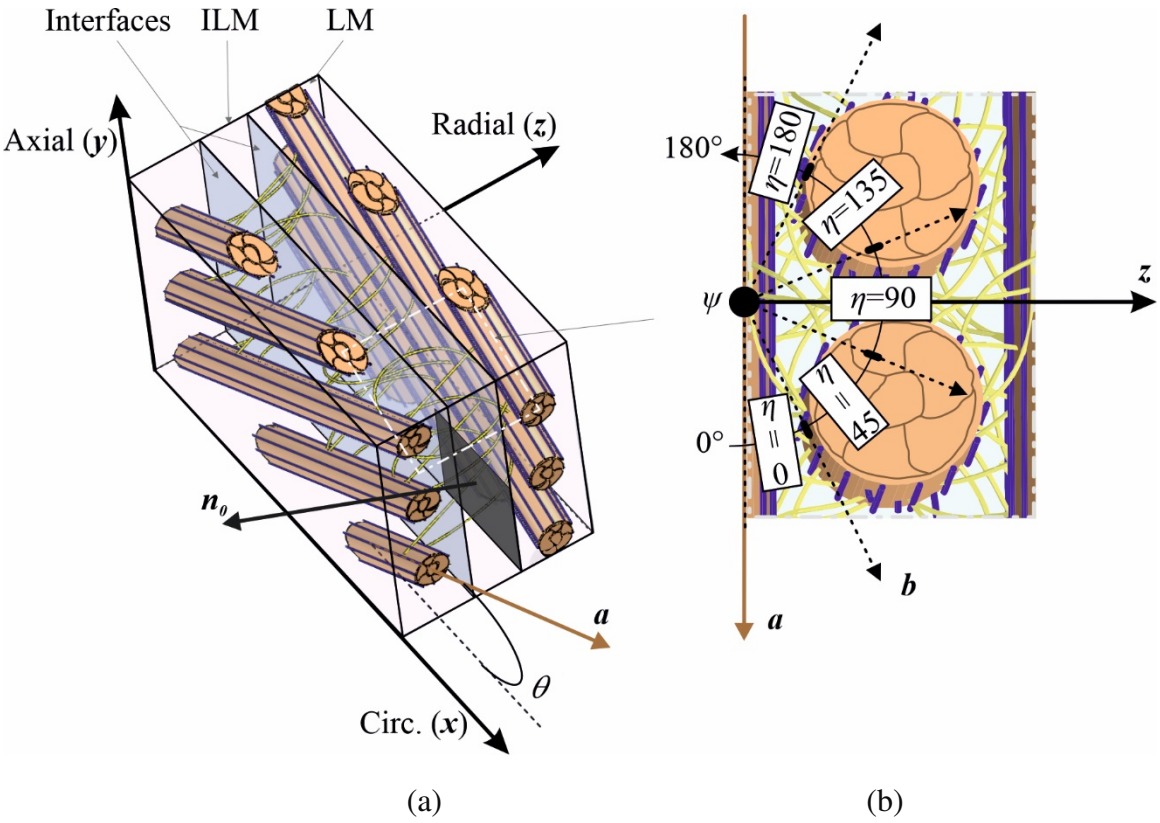

(a) (b)

Figure 2. Coordinate systems of (a) the multi-layered material element ($\boldsymbol{n_0}$-axis is the unit vector at inter-layer interfaces and $\boldsymbol{a}$-axis is the unit vector along OCF that forms an angle θ with the $\boldsymbol{x}$-axis) and (b) of the five NEF bundles $\eta = \{0°, 45°, 90°, 135°, 180°\}$ ($\boldsymbol{b}$-axis is the unit vector along NEF that forms an angle y with the $\boldsymbol{a}$-axis).

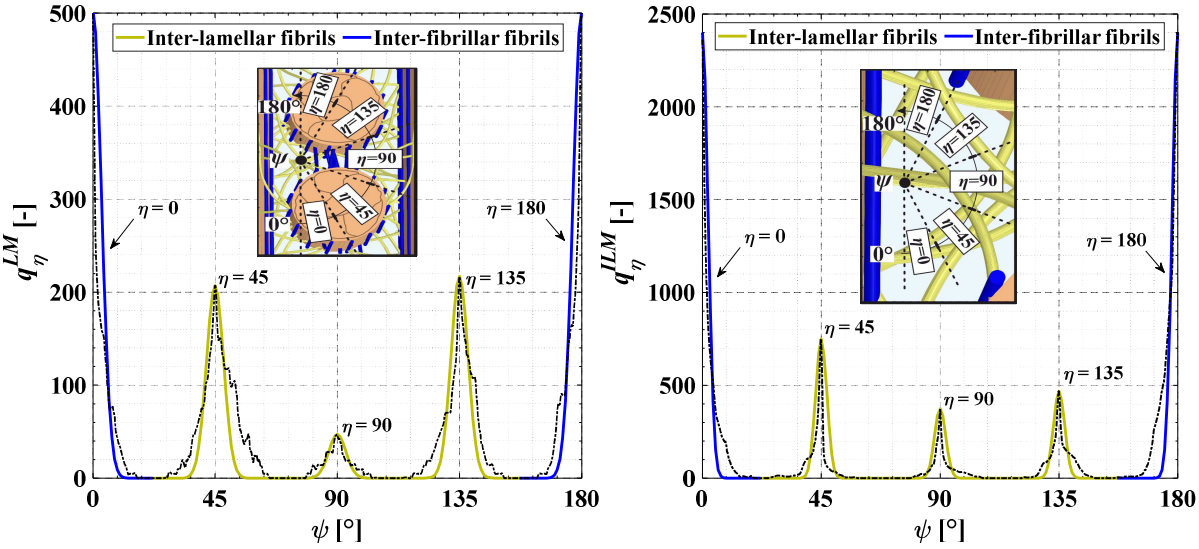

(a) (b)

Figure 3. Quantity of NEF (a) in LM and (b) in ILM; continuous lines: Eq. (3), dashed lines: experimental data [11].

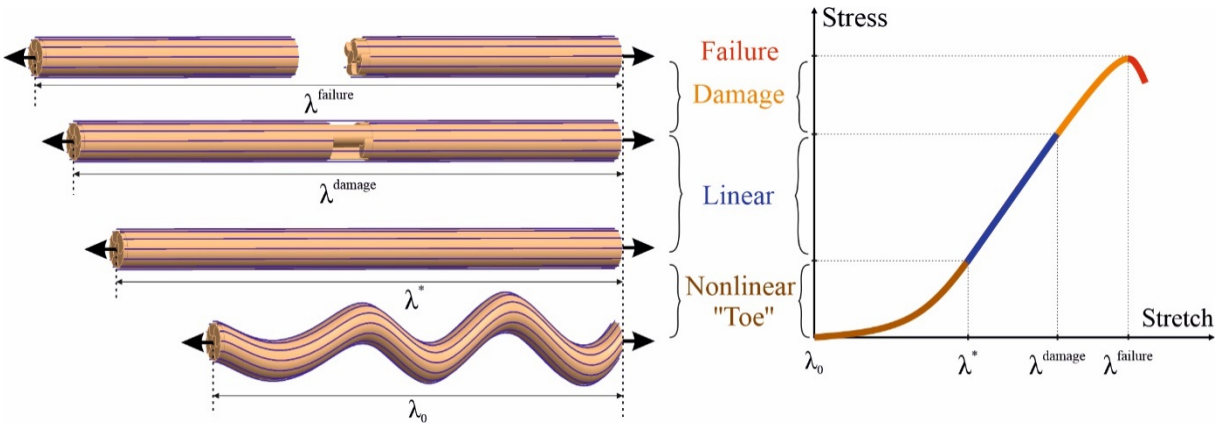

Figure 4. Behavior of a single collagen fiber stretched until failure.

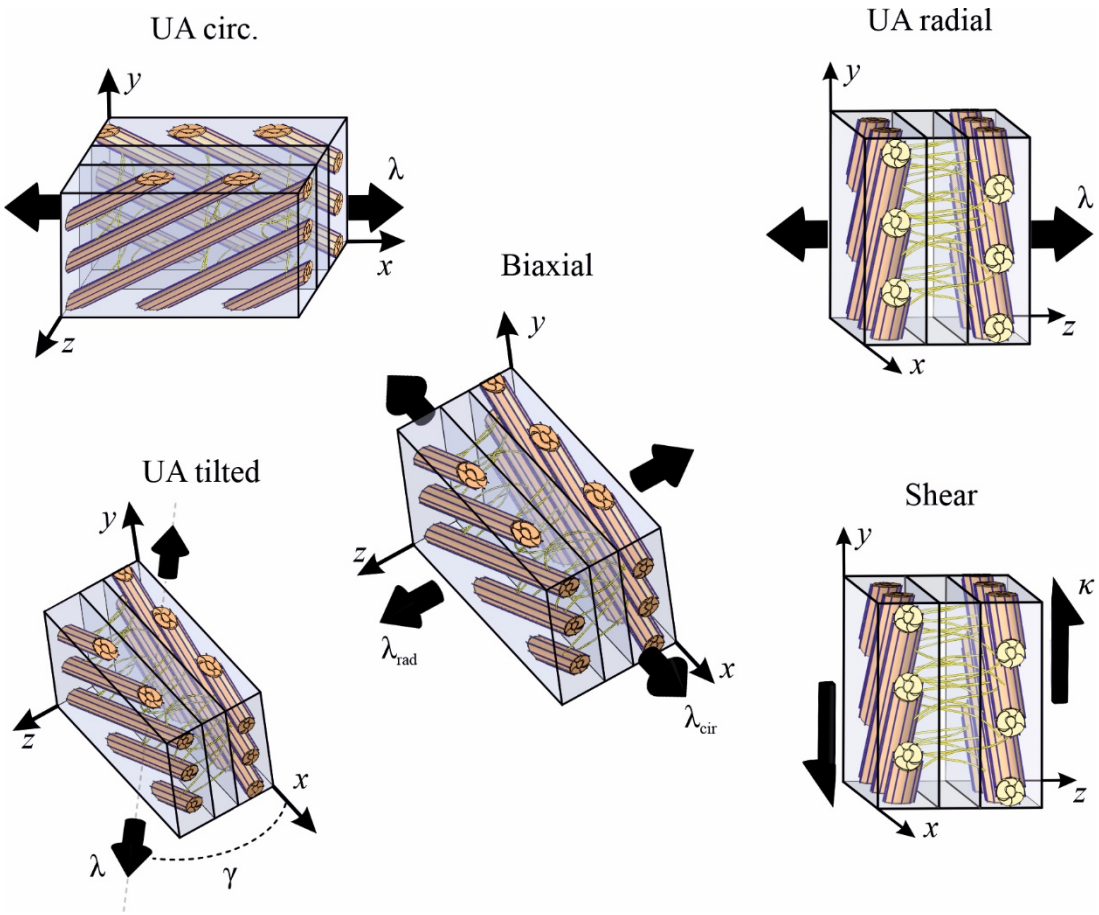

Figure 5. Loading paths applied on the multi-layered material element.

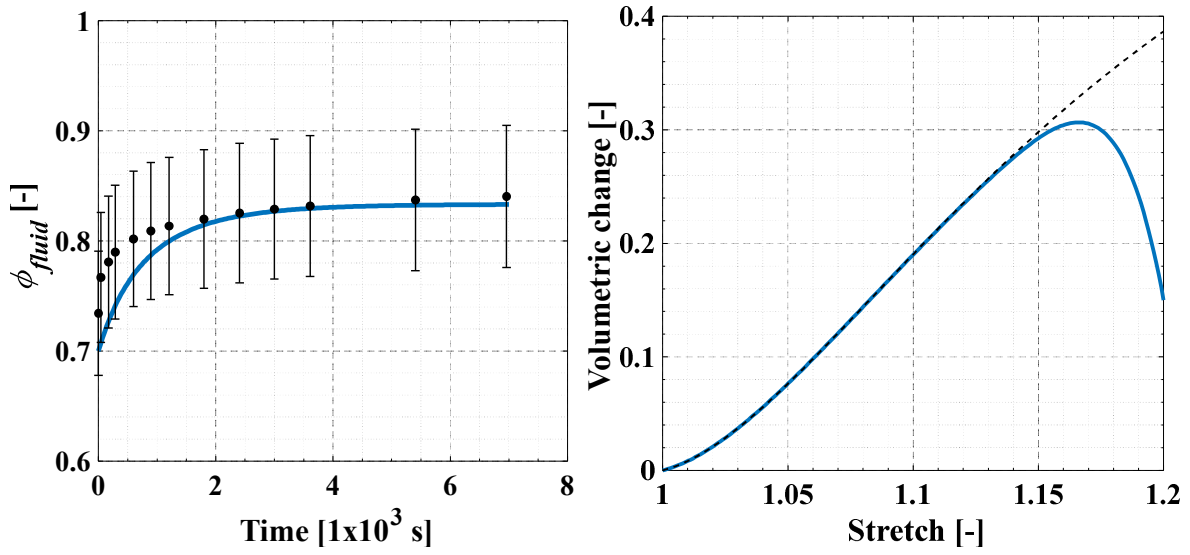

(a) (b)

Figure 6. Volumetric response of the multi-layered material element: (a) under free swelling (line: model, symbol: experimental data of Acaroglu et al. [51]), (b) under UA circumferential stretching (solid line: model, dashed line model without damage).

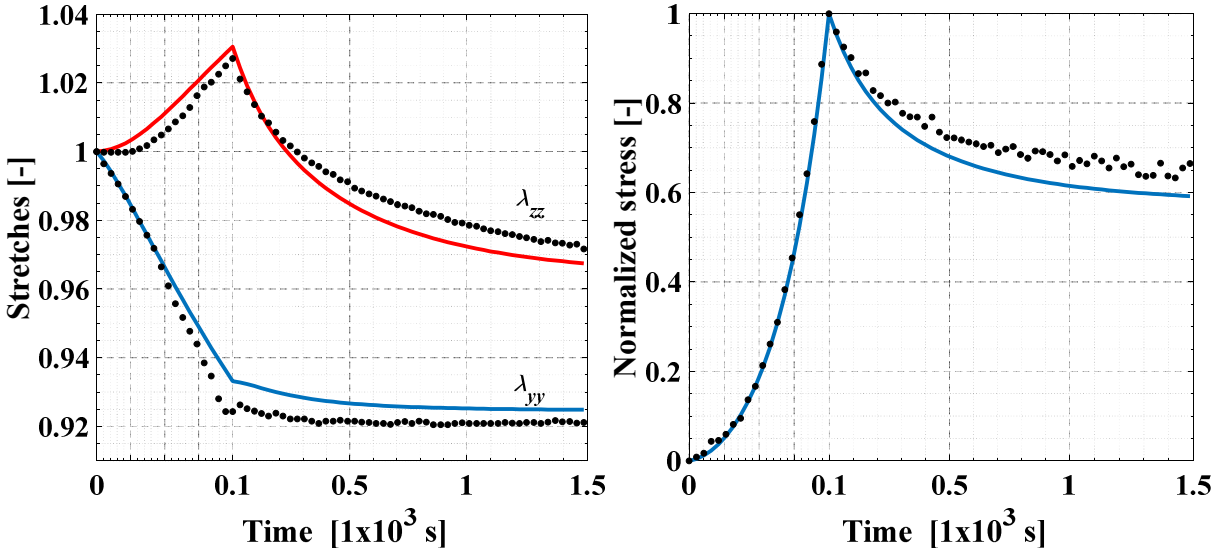

(a) (b)

Figure 7. Temporal changes of (a) transversal stretches and (b) normalized stress of the multi-layered material element under a UA circumferential stretching until 1.1 followed by a relaxation (lines: model, symbols: experimental data of Baldit [53]).

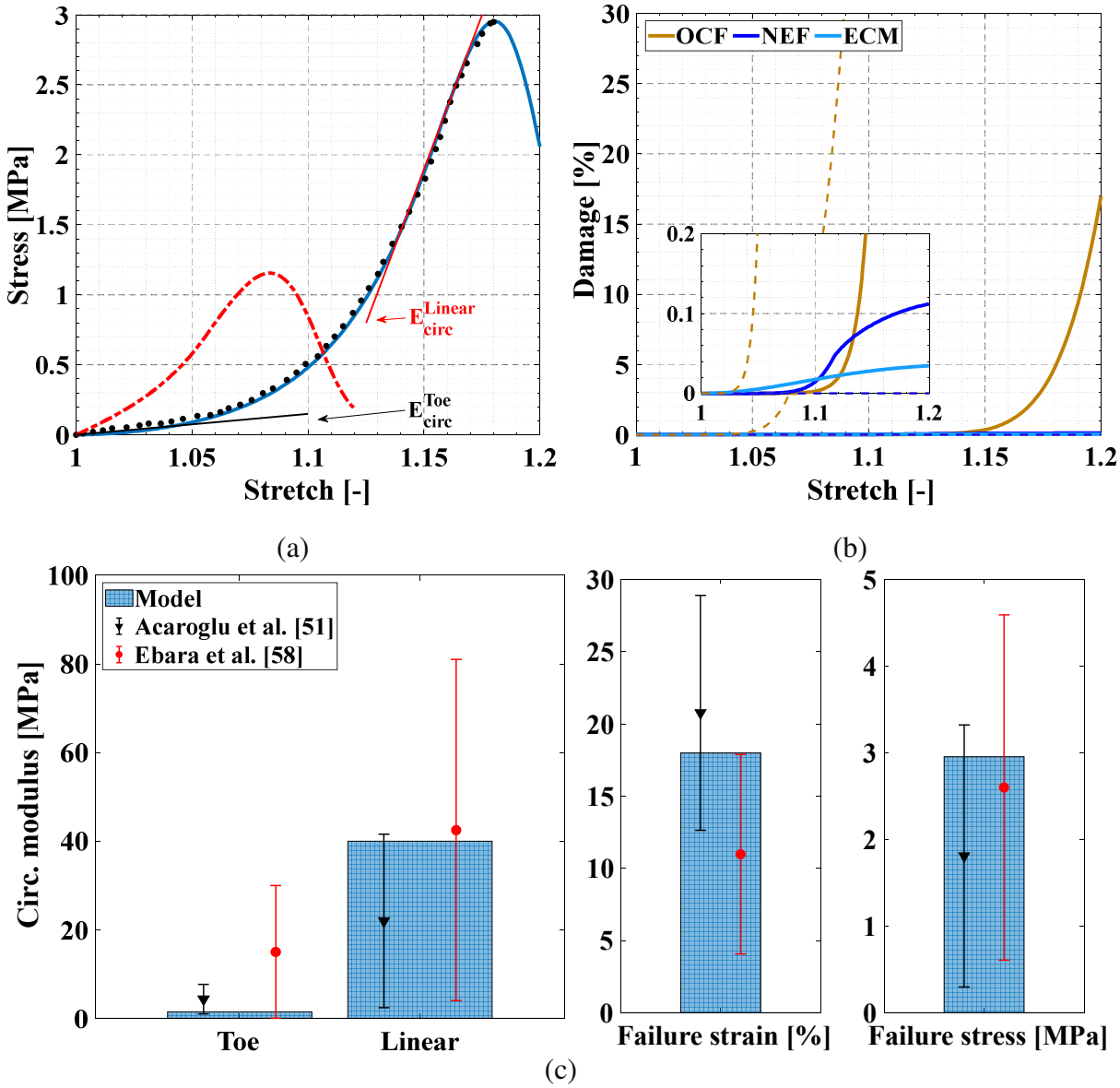

Figure 8. UA circumferential stretching of the multi-layered material element: (a) stress-stretch response (solid line: model; dashed line: model without chemical effect, symbols: experimental data of Acaroglu et al. [51]), (b) local damage events in the different solid constituents (solid line: model; dashed line: model without chemical effect), (c) toe and linear circumferential moduli, failure strain and failure stress.

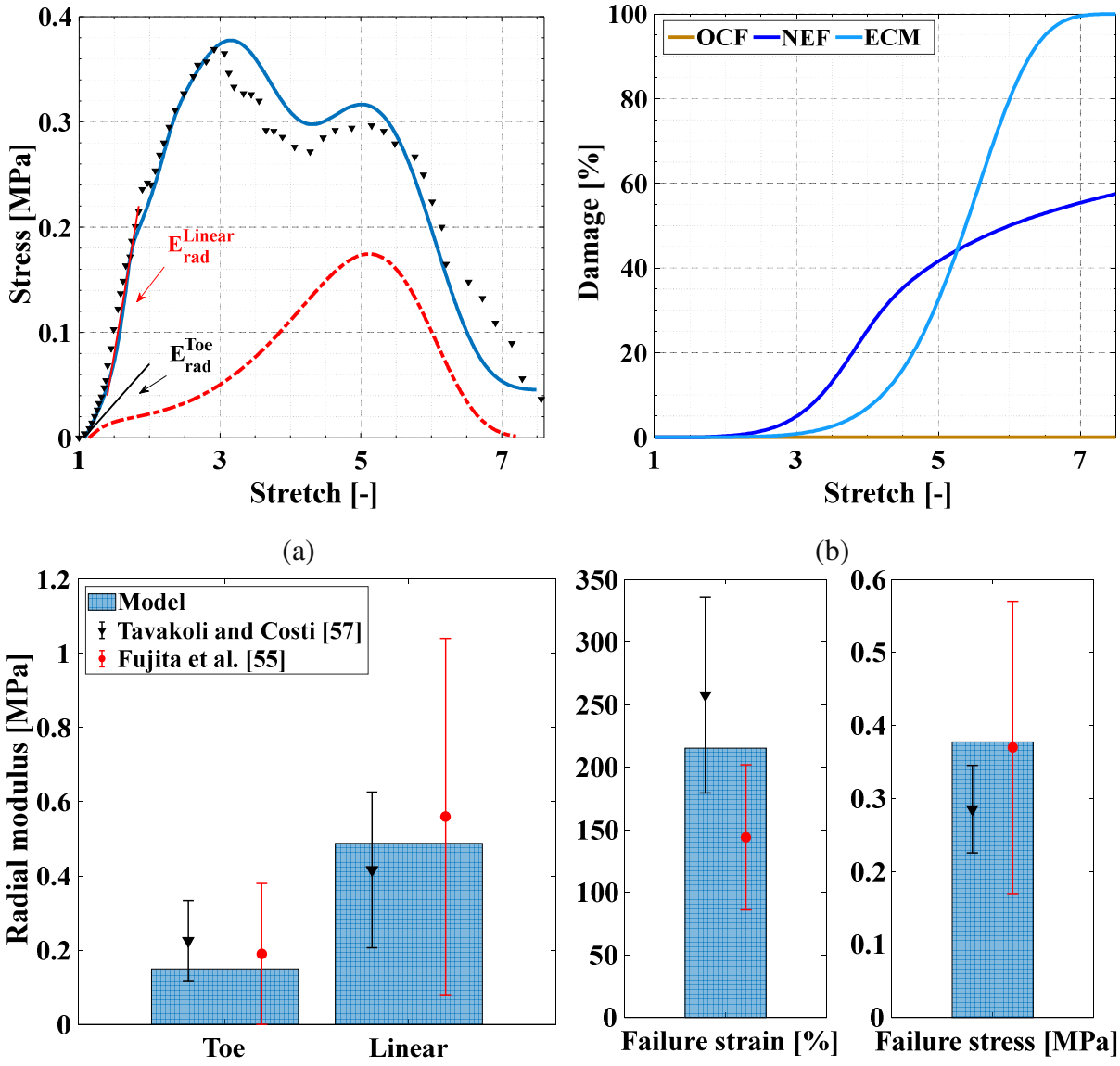

Figure 9. UA radial stretching of the multi-layered material element: (a) stress-stretch response (solid line: model; dashed line: model without NEF activation, symbols: experimental data of Tavakoli and Costi [57]), (b) local damage events in the different solid constituents, (c) toe and linear radial moduli, failure strain and failure stress.

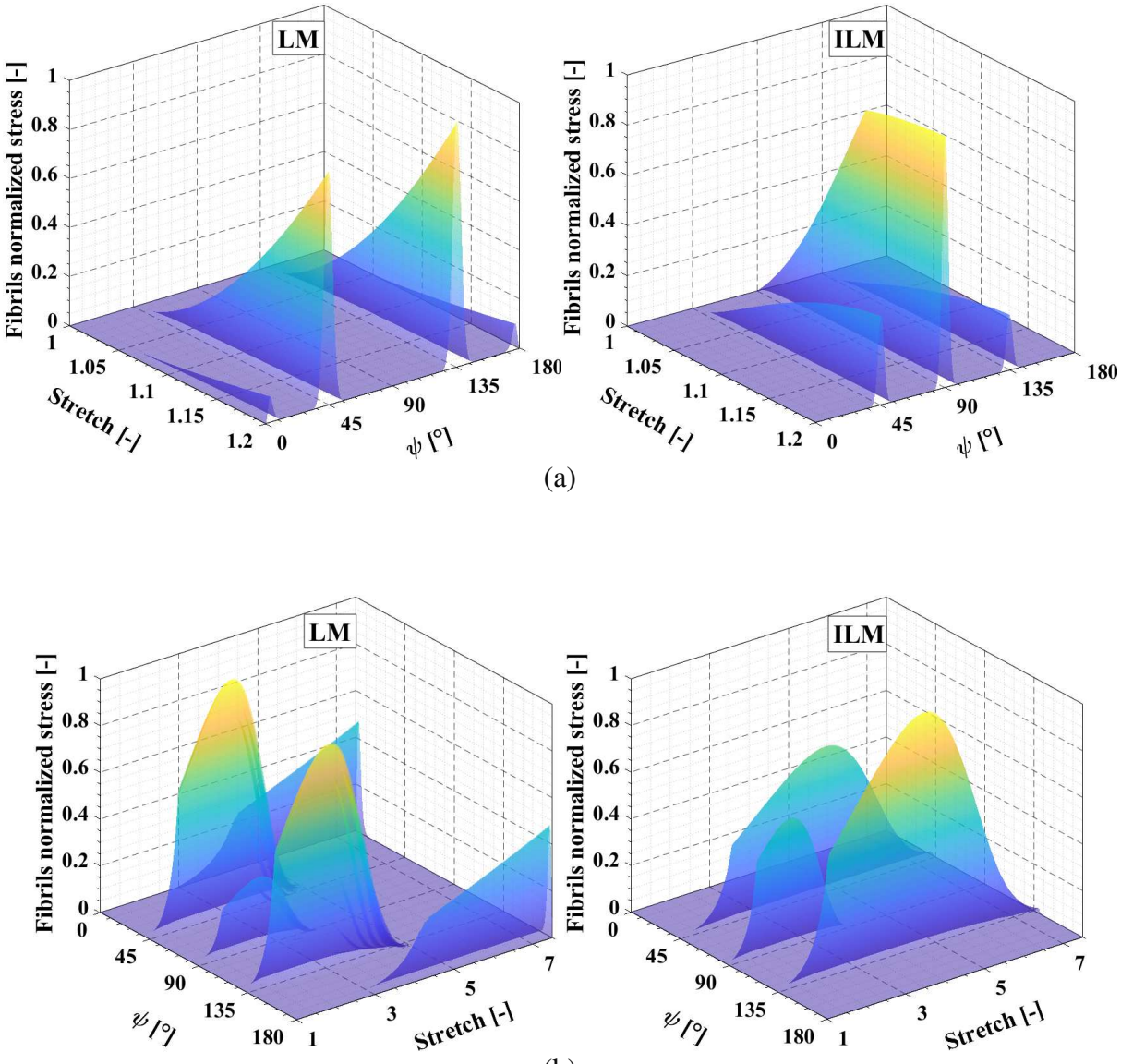

Figure 10. Local NEF stress maps under (a) UA circumferential stretching and (b) UA radial stretching.

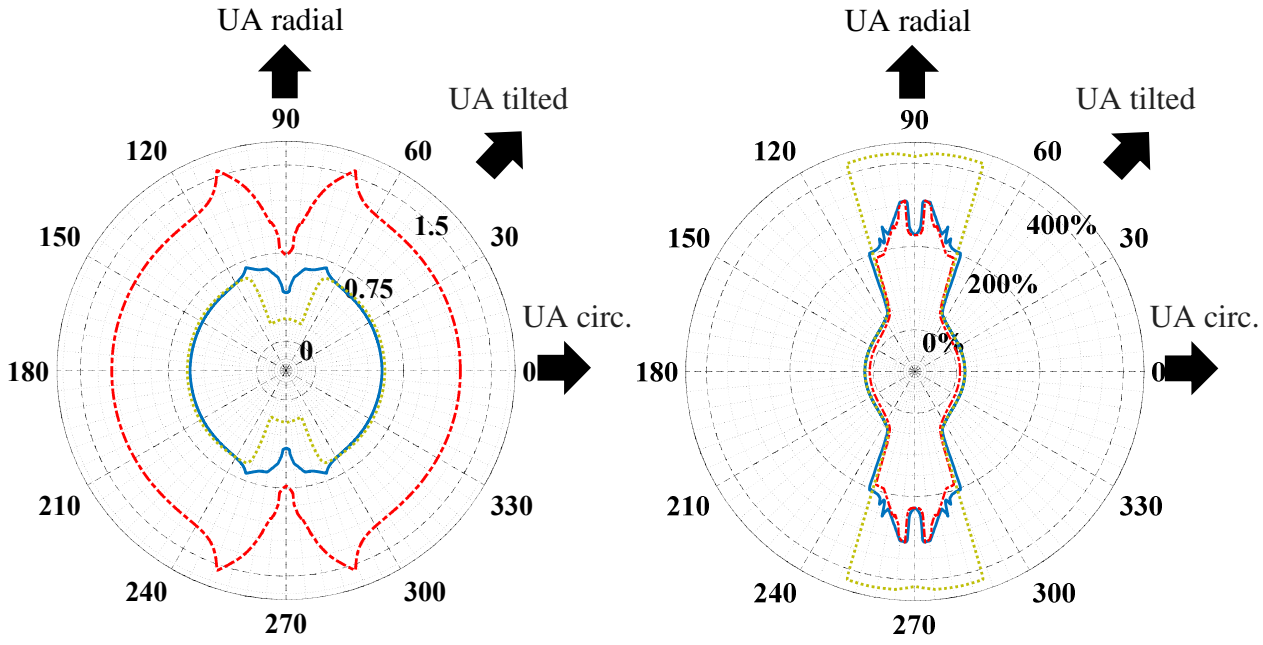

(a) (b)

Figure 11. UA failure envelopes: (a) effective stress [MPa] and (b) maximum principal strain [%] (continuous blue line: model, dashed yellow line: model without NEF, dashed red line: model without chemical effect).

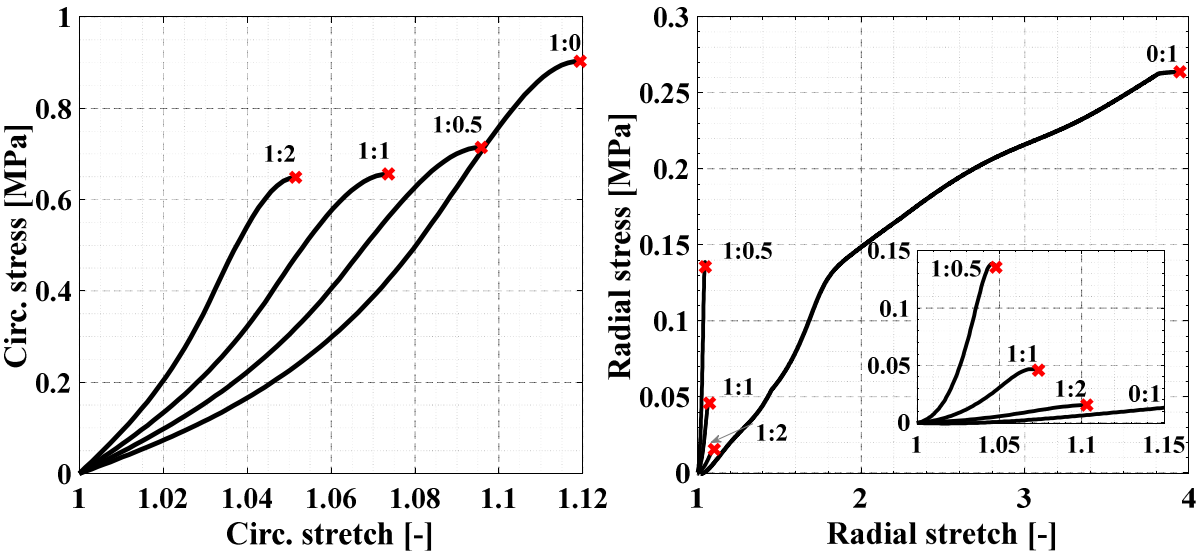

(a) (b)

Figure 12. Biaxial stretching of the multi-layered material element for different biaxiality ratios: (a) circumferential stress-stretch response, (b) radial stress-stretch response.

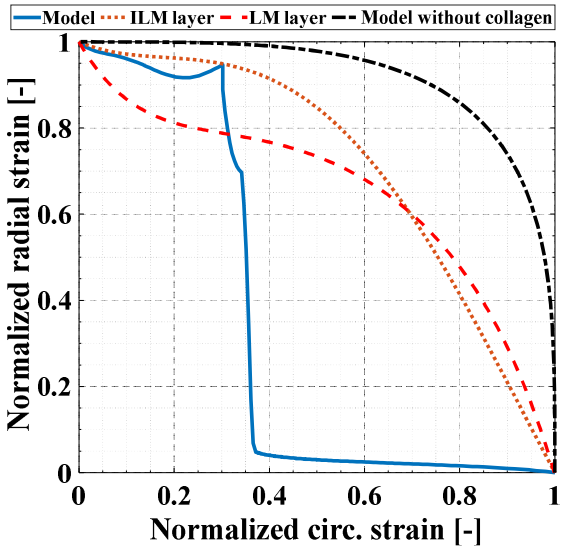

Figure 13. Biaxial failure envelope.

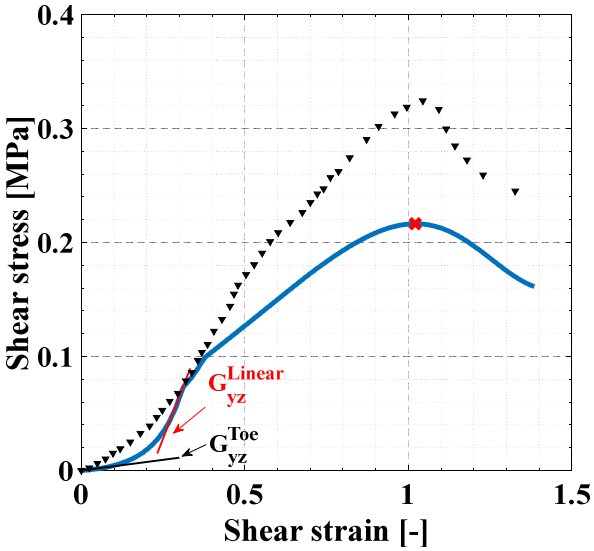

Figure 14. Shearing of the multi-layered material element (continuous line: model, symbols: experimental data of Tavakoli and Costi [57]).

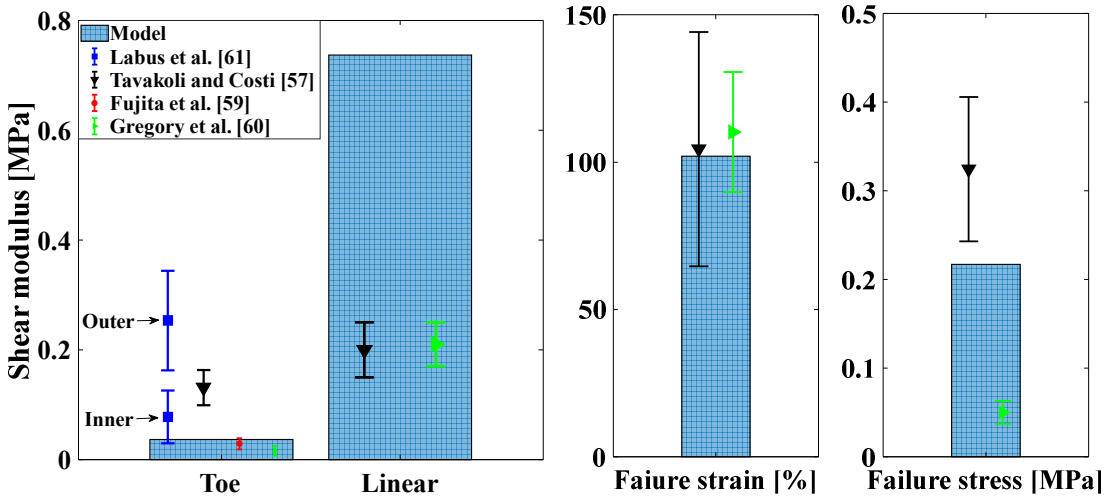

(a) (b) (c)

Figure 15. Shearing of the multi-layered material element: (a) Toe and linear shear moduli, (b) failure strain and (c) failure stress.

Parameters	Values		References
z_{max}	0.76	$[\mathrm{mm}]$	[52]
z_{min}	0.69	$[\mathrm{mm}]$	[52]
$r_{ILM/LM}$	0.133	$[-]$	[11]
θ	30	$[\mathrm{deg}]$	[52, 53]
$\phi_{collagen}$	0.07	$[-]$	[50]
ϕ_{fluid_0}	0.7	$[-]$	[51]

Table 1. Structural parameters.

	Components	Parameters	Values	
Swelling	Fluid	K_1	0.14	$[\mathrm{MPa}]$
		K_2	0.075	$[-]$
Toe	ECM	G_{ECM}	0.01	$[\mathrm{MPa}]$
	OCF	C_1	26	$[\mathrm{MPa}]$
		C_2	12	$[-]$
	NEF	C_4	25	$[\mathrm{MPa}]$
		C_5	0.2	$[-]$
Linear	OCF	C_3	70	$[\mathrm{MPa}]$
		λ^*_{OCF}	1.09	$[-]$
	NEF	C_6	1.5	$[\mathrm{MPa}]$
		λ^*_{FCN}	1.7	$[-]$
Damage	ECM	α_{ECM}	2	$[-]$
		β_{ECM}	5.5	$[\mathrm{MPa}]$
	OCF	α_{OCF}	5	$[-]$
		β_{OCF}	43	$[\mathrm{MPa}]$
	NEF	α_{fl}	6	$[-]$
		β_{fl}	850	$[\mathrm{MPa}]$

Table 2. Model parameters.

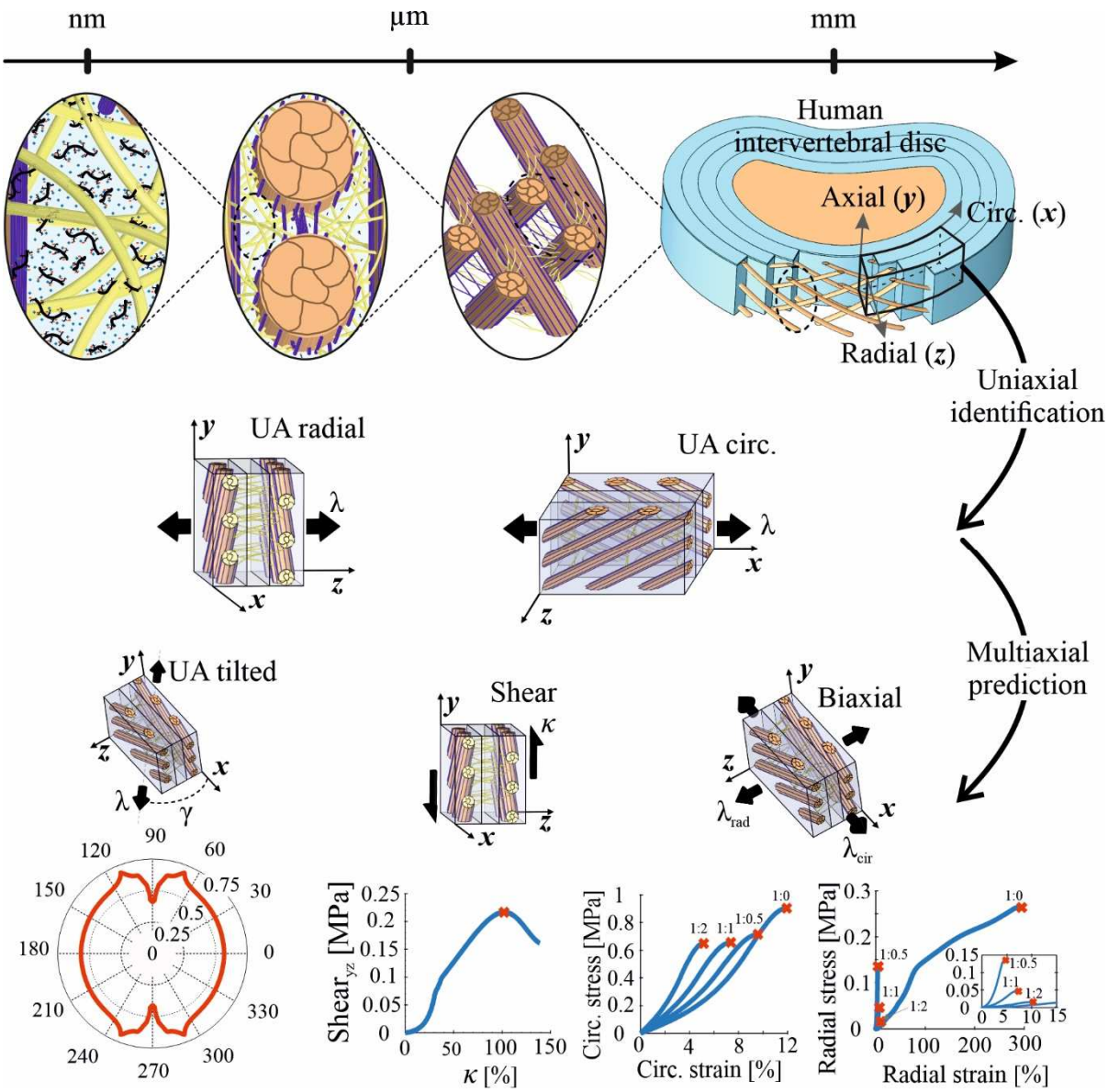
nm
µm
mm
Human intervertebral disc
Axial (y)
Circ. (x)
Radial (z)
Uniaxial identification
UA radial
UA circ.
Multiaxial prediction
UA tilted
Shear
Biaxial
Shear$_{yz}$ [MPa]
κ [%]
Circ. stress [MPa]
Circ. strain [%]
Radial stress [MPa]
Radial strain [%]
1:0
1:0.5
1:1
1:2